MODELLISTICA E CALCOLO SCIENTIFICO

MOX

MODELING AND SCIENTIFIC COMPUTING

MOX-Report No. 78/2023

Discontinuous Galerkin for the heterodimer model of prion dynamics in Parkinson's disease

Antonietti, P.F.; Bonizzoni, F.; Corti, M.; Dall'Olio, A.

Discontinuous Galerkin for the heterodimer model of prion dynamics in Parkinson's disease*

Paola F. Antonietti[1], Francesca Bonizzoni[1], Mattia Corti[1], and Agnese Dall'Olio[1]

[1] *MOX-Dipartimento di Matematica, Politecnico di Milano, Piazza Leonardo da Vinci 32, Milan, 20133, Italy*

October 12, 2023

Abstract

Neurodegenerative diseases have a significant global impact affecting millions of individuals worldwide. Some of them, known as proteinopathies, are characterized by the accumulation and propagation of toxic proteins, known as prions. Alzheimer's and Parkinson's diseases are relevant of protheinopathies. Mathematical models of prion dynamics play a crucial role in understanding disease progression and could be of help to potential interventions. This article focuses on the heterodimer model: a system of two partial differential equations that describe the evolution of healthy and misfolded proteins. In particular, we propose a space discretization based on a Discontinuous Galerkin method on polygonal/polyhedral grids, which provides flexibility in handling meshes of complex brain geometries. Concerning the semi-discrete formulation we prove stability and a-priori error estimates. Next, we adopt a ϑ-method scheme for time discretization. Some convergence tests are performed to confirm the theoretical bounds and the ability of the method to approximate travelling wave solutions. The proposed scheme is also tested to simulate the spread of α-synuclein in a realistic test case of Parkinson's disease in a two-dimensional sagittal brain section geometry reconstructed from medical images.

1 Introduction

Neurodegenerative diseases have a significant global impact affecting millions of people worldwide. Despite different manifestations and a wide spectrum of symptoms among neurodegenerative diseases, many of them can be collectively categorized as proteinopathies due to compelling evidence indicating that their progression is closely linked to the aggregation of specific toxic proteins, commonly referred to as prions [1]. Remarkable examples of proteinopathies are Alzheimer's and Parkinson's diseases. Alterations in the protein's structure result in the corruption of its characteristic and functional properties, rendering it unable to fulfil its intended role. Complications arise when the misfolded structure exhibits age-related resistance to the clearance mechanism [2], impeding its elimination and leading to the tendency to accumulate in agglomerates, which in the end cause the neurons' death [3].

Once present in the organism, a key aspect of prions is that they act as templates to induce the misfolding and aggregation of otherwise healthy proteins, thereby propagating the disease [4]. A direct correlation can be established between the microscopic phenomena involving prion-like proteins and the manifestation of certain observable symptoms [5]. These phenomena typically span over decades, making on the one hand clinical observations very complex and on the other hand the development of mathematical and computational models a key instrument to asses patient-specific evolution scenarios.

In the particular case of Parkinson's disease, α-synuclein evolution assumes a pivotal role: α-synuclein is a protein predominantly localized within presynaptic nerve terminals, whose physiological functions are still not completely understood. Nevertheless, there is evidence suggesting its potential involvement in neurons' interconnections [6]. α-Synuclein monomers undergo polymerization, leading to the formation of extended filaments. During this phase abnormal mutations may arise, resulting in the creation of insoluble filamentous inclusions, known as Lewy bodies [7]. Lewy bodies are recognized as hallmark lesions found in the brains of individuals suffering from Parkinson's disease, marking the degeneration of neurons. Hence, therapeutic approaches aimed at mitigating the misfolding of

these proteins constitute a topic of paramount significance within contemporary medical research [4], as well as the construction of chemical ligands for positron emission tomography imaging (PET) which do not exist nowadays [8]. Moreover, elaborating a sophisticated mathematical representation of its evolution would provide valuable insights into the disease progression [9], since the detection of such protein is only possible by histological examination of postmortem brain tissue [8]. A comprehensive review of the mathematical models proposed to describe the prions dynamics can be found in [10].

In this work, we focus on the numerical modelling of the heterodimer continuum model [11]. This model is formulated as a system of two non-linear diffusive partial differential equations (PDEs). Its objective is to describe the underlying microscopic mechanism of prion dynamics while capturing the broader macroscopic phenomenon of prion propagation throughout the designated spatial domain. This approach embraces a complete consideration of both the healthy and misfolded protein configurations, affording deep insights into the mechanistic aspects of infections.

In this context, the typical model which is used, under the assumption of constant healthy prion concentration is the Fisher-Kolmogorov (FK) equation [12]. The two models are related since, through mathematical considerations, it is possible to reduce the coupled system of equations inherent to the heterodimer model into the FK equation, which describes the evolution of the relative concentration of misfolded protein, in the simplest possible way [13]. Although it is more complex compared to the FK equation, the heterodimer model justifiably warrants the additional computational effort. This is attributable to the possibility of analyzing a more informative solution, as it explicitly accommodates the dynamic evolution of healthy proteins alongside the misfolded counterparts. Furthermore, the explicit inclusion of terms representing distinct molecular kinetic processes—namely, production, destruction, and conversion- affords the ability to simulate diverse scenarios [14]. Finally, the study and numerical simulation of the heterodimer model serves as an intermediate step toward a more general comprehension of prions pathogenesis, fully described by the more advanced Smoluchowski model [15], where the concentrations of polymers of different sizes are followed independently. Therefore, the heterodimer model constitutes a natural balance between computational complexity and physical insights into the prion dynamics.

Concerning the numerical approximation of the heterodimer model, in literature we find many different methods, i.e. finite element methods [14] or reduced order network diffusion models [16]. In this work, we propose and analyze a Discontinuous Galerkin formulation on polygonal/polyhedral grids (PolyDG) for the space discretization of the heterodimer system, coupled with a Crank-Nicolson time discretization scheme, with semi-implicit treatment of the nonlinear term. For this method, we derive also in this work stability and *a-priori* error estimate for the semidiscrete formulation. To the best of our knowledge, these are the first results of this type for the semidiscrete form of the heterodimer model.

The proposed approach enjoys distinguishing features compared to the available approaches in the literature. For example, it supports high-order approximations able to correctly reproduce travelling-wave solutions. Leveraging the PolyDG method, we attain a substantial degree of flexibility in addressing the complexities of geometry, thanks to the possibility of exploiting agglomeration techniques. PolyDG methods allow also local adjustment of the discretization parameters, such as polynomial order (*p*-refinement) and element diameter (*h*-refinement) [17]. PolyDG's adaptability becomes particularly advantageous in the accurate approximation of propagating wavefronts, even within meshes not excessively refined. Within this context, PolyDG methodology further enhances the versatility and generality of the approach, concerning arbitrarily shaped elements. This gives great flexibility also in the construction of the mesh, thanks to the possibility of mesh agglomeration [18]. The procedure consists of constructing a coarse mesh starting from an original highly refined triangulation, necessitated for the accurate representation of the complex structure and details of the brain's geometry. The agglomerated grid now comprises generic polygons, maintaining the original boundary details without requiring curved elements. This restructuring causes a noteworthy reduction in computational cost.

The paper is organized as follows. Section 2 presents the heterodimer model, then Section 3 is dedicated to deriving the PolyDG formulation. In Section 4 we prove stability and *a-priori* error estimates and in Section 5 we present the fully discrete formulation of the problem. In Section 6 theoretical convergence rates are verified via numerical simulations with analytical solutions and the ability of the model to reproduce a travelling-wave solution is demonstrated. In Section 7, we simulate the spreading of α-synuclein protein within a two-dimensional brain section. Finally, in Section 8, we draw some conclusions and discuss future developments.

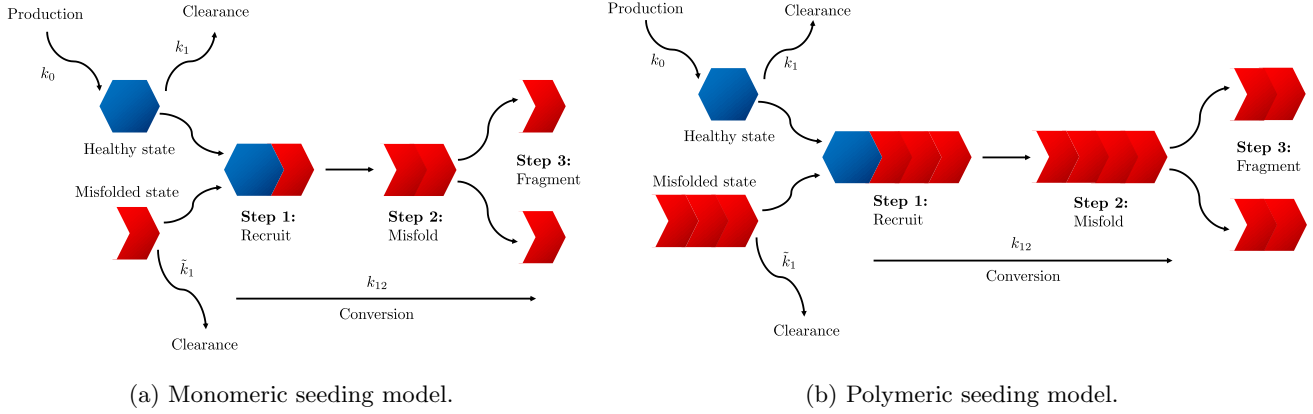(a) Monomeric seeding model.　　　　　　　　(b) Polymeric seeding model.

Figure 1: Schematic representation of monomeric and polymeric seeding models.

2　The mathematical model

The mathematical formulation employed to address the kinetics of prion pathogenesis incorporates the representation of both prion conversion dynamics and the spatial dissemination of these infectious agents within the reference domain. By employing this formulation, a coherent link is established between the microscopic-level kinetic model and the observable macroscopic manifestations of anisotropic diffusion pertaining to pathogenic microorganisms. Proteinopathies involve a multitude of interconnected phenomena at various scales, all of which play significant roles in the progression of the pathology, like biochemical reactions at a microscopic scale and accumulation of misfolded proteins agglomerating over entire areas of the brain, causing neurons' death and the consequent manifestations of the disease characteristic symptoms.

Despite the fact that the prion conversion mechanism remains poorly understood, one of the simplest employed approach to explain the interactions between prions and prionic proteins is the heterodimer model, initially proposed by [19, 20]. According to this model, a prion molecule tends to interact with the healthy prion protein forming a heterodimer molecule, then, due to biochemical mechanisms that have not been fully elucidated yet, the prion protein is converted into its misfolded version, and the resulting polymer fragments into two singular prions that will continue to act as infectious seed and spread (see Figure 1a).

An extension of the aforementioned heterodimer model is the nucleated polymerization model by Harper and Lansbury [21], initially proposed to describe the seeding of β-amyloid in Alzheimer's disease, but whose concepts can be extended to general prion proteins like α-synuclein. According to their theory, misfolded proteins exhibit a tendency to react within themselves [22]. Therefore, it is more likely to find them in the form of short polymer that corrupts healthy proteins, fragments into several misfolded proteins, or aggregates to form amyloids (see Figure 1b). In the present model, this conversion process is summarized in a single step characterized by rate constant, denoted in the following by k_{12}, and proportional to the concentration of both healthy and misfolded proteins [13].

The equations that govern the description of the spatial and temporal dynamics of the overall quantity of healthy $c(\boldsymbol{x}, t)$ and misfolded $q(\boldsymbol{x}, t)$ proteins within an open bounded domain $\Omega \in \mathbb{R}^d$ ($d = 2, 3$) with Lipschitz boundary, over a time interval $(0, T]$ is the following:

$$
\begin{cases}
\dfrac{\mathrm{d}c}{\mathrm{d}t} = \nabla \cdot (\mathbf{D}\nabla c) - k_1\, c - k_{12}\, c\, q + k_0 + f_c & \text{in } \Omega \times (0, T], \\[2mm]
\dfrac{\mathrm{d}q}{\mathrm{d}t} = \nabla \cdot (\mathbf{D}\nabla q) - \tilde{k}_1\, q + k_{12}\, q\, c + f_q & \text{in } \Omega \times (0, T], \\[2mm]
c = c_{\mathrm{D}}, \quad q = q_{\mathrm{D}} & \text{on } \partial\Omega_{\mathrm{D}} \times (0, T], \\[2mm]
(\mathbf{D} \cdot \nabla c) \cdot \mathbf{n} = 0, \quad (\mathbf{D} \cdot \nabla q) \cdot \mathbf{n} = 0 & \text{on } \partial\Omega_{\mathrm{N}} \times (0, T], \\[2mm]
c(0, \boldsymbol{x}) = c_0, \quad q(0, \boldsymbol{x}) = q_0 & \text{in } \Omega.
\end{cases}
\tag{1}
$$

The model takes the form of a time-dependent system of PDEs coupled through a non-linear reaction term. Healthy proteins are assumed to be naturally produced by the organism at a rate $k_0 \geq 0$, their concentration is affected by a biological destruction process at a rate $k_1 \geq 0$, whereas they are converted into prions as previously described at rate $k_{12} \geq 0$. In contrast, misfolded proteins undergo a clearance mechanism characterized by a rate $\tilde{k}_1 \geq 0$.

However, due to their distinct structural conformation, these proteins exhibit insolubility and enhanced resistance to the biological elimination process that typically occurs when generic proteins misfold. The forcing terms $f_c(\boldsymbol{x}, t)$ and $f_q(\boldsymbol{x}, t)$ correspond to a generic external introduction of mass into the system, which is often neglected in the applications. Suitable initial and boundary conditions complete the model. The boundary of the domain $\partial\Omega$ is partitioned into two disjoint subsets, namely $\partial\Omega_D$ and $\partial\Omega_N$. On $\partial\Omega_D$, we impose fixed concentration values, while on $\partial\Omega_N$, we enforce zero flux conditions, with $\boldsymbol{n}$ denoting the normal vector pointing outward from the domain. The initial conditions $q_0(\boldsymbol{x})$ and $c_0(\boldsymbol{x})$ correspond to infectious and healthy proteins initial concentrations, respectively.

From a macroscopic perspective, the propagation of proteins throughout the domain is captured by the diffusion term in Equation (1). The spreading of proteins within the brain occurs via two main mechanisms, extracellular diffusion and axonal transport, and can be mathematically characterized by employing the diffusion tensor defined as follows [13]:

$$\mathbf{D}(\boldsymbol{x}) = d_{\text{ext}}\mathbf{I} + d_{\text{axn}}\bar{\boldsymbol{a}}(\boldsymbol{x}) \otimes \bar{\boldsymbol{a}}(\boldsymbol{x}), \tag{2}$$

where the second term models the anisotropic diffusion of substances along the axonal directions, denoted by the vector $\bar{\boldsymbol{a}}(\boldsymbol{x})$, which is proportional to $d_{\text{axn}} > 0$. It is commonly assumed that the axonal transport is faster than the isotropic extracellular diffusion, therefore $d_{axn} \geq d_{ext} > 0$ [13].

Assumption 1. *For the subsequent analysis of the problem we require a certain regularity for the data, forcing terms and boundary conditions:*

- $\mathbf{D} \in L^\infty(\Omega, \mathbb{R}^{d \times d})$ *and* $\exists d_0 > 0: d_0|\boldsymbol{\xi}|^2 \leq \boldsymbol{\xi}^\top \mathbf{D}\boldsymbol{\xi} \quad \forall \boldsymbol{\xi} \in \mathbb{R}^d$;

- $k_0, k_1, \tilde{k}_1, k_{12} \in L^\infty_+(\Omega)$;

- $f_c(\boldsymbol{x}, t), f_q(\boldsymbol{x}, t) \in L^2((0, T]; L^2(\Omega))$;

- $c_D, q_D \in L^2((0, T], H^{1/2}(\partial\Omega_D))$.

By analyzing the steady-state solutions of (1), it can be proved that the model exhibits two distinct equilibria. The first is an unstable equilibrium at $c = k_0/k_1$ and $q = 0$, representing a healthy condition where no misfolded proteins are present. The second equilibrium $c = \tilde{k}_1/k_{12}$ and $q = k_0/\tilde{k}_1 - k_1/k_{12}$ is stable and corresponds to a situation where both protein species coexist. This implies that even a small non-zero quantity of misfolded proteins, whether due to the spontaneous conversion of healthy proteins (which is rather unlikely, as noted in [23]) or the presence of external infectious agents in the form of initial condition q_0, can initiate an irreversible chain reaction of conversion and spread. Furthermore, for the observation of a travelling-wave solution, transitioning the system towards a pathological state, it is crucial for the coefficients of Equations (1) to adhere to a specific relationship [16]:

$$k_0 k_{12} - \tilde{k}_1 k_1 > 0. \tag{3}$$

Failure to satisfy this condition would result in having a stable equilibrium point in the healthy state implying that the model is not well suited for describing the diffusion of pathogenic prions. If Equation (3) holds and assuming isotropic diffusion, the wave speed for concentrations of unhealthy prions can be computed analytically [11]:

$$\bar{v} = \sqrt{d_{ext}k_{12}\left(\frac{k_0}{k_1} - \frac{\tilde{k}_1}{k_{12}}\right)}. \tag{4}$$

3 Polytopal discontinuous Galerkin semi-discrete formulation

In this section, we aim to present the spatial discretization of Equation (1) using the PolyDG method [17, 24, 25, 26]. To ease the exposition of the discrete framework, we initially introduce preliminary definitions, mesh assumptions, and relevant estimates. Moreover, we introduce the symbol $x \lesssim y$ to mean that $\exists C > 0: x \leq Cy$, where C may depend on model parameters and the degree of polynomial approximation denoted as p, but it is independent of the mesh-size h.

3.1 Discrete setting: polytopal meshes and functional spaces

We introduce a partition $\mathscr{T}_h$ over the domain Ω, consisting of non-empty, disjoint polygonal or polyhedral elements. Each mesh element $K \in \mathscr{T}_h$ is associated with its measure denoted as $|K|$, and its diameter denoted as h_K, defined

as the upper bound of the distances between any pair of points within K. Consequently, the mesh size parameter is defined as $h = \max_{K \in \mathscr{T}_h} \{h_K\}$.

Additionally, we consider a partition $\mathscr{F}_h$ of the mesh skeleton, which consists of disjoint $(d-1)$-dimensional subsets of Ω known as mesh faces F. These faces are defined in such a way that each face is either an interface between two distinct elements $T_1, T_2 \in \mathscr{T}_h$ (where $F \subset T_1 \cap T_2$), or a boundary face (where $F \subset T_1 \cap \partial\Omega$). This general definition implies that mesh interfaces do not necessarily coincide with the faces of polytopic elements in the partition $\mathscr{T}_h$, allowing for the handling of non-conforming partitions that involve hanging nodes. Moreover, it accommodates partitions where the faces may not be planar or even connected, thereby providing greater flexibility for the method's applicability [27].

In the two-dimensional setting $(d = 2)$, mesh faces correspond to line segments. In three-dimensional domains, mesh faces consist of general polygonal surfaces that are further assumed to be subdivided into triangles. Henceforth, $\mathscr{F}_h$ will denote the collective set of mesh faces or all open triangles belonging to a sub-triangulation of the mesh faces in three-dimensional domains. Consequently, $\mathscr{F}_h$ is consistently defined as a set of $(d-1)$-dimensional simplexes. The set $\mathscr{F}_h$ can be subdivided into two distinct subsets: $\mathscr{F}_h^{\mathrm{I}}$, that comprises all interior interfaces, and $\mathscr{F}_h^{\mathrm{B}}$, that consists of all boundary faces. The boundary faces can be further partitioned based on the type of boundary conditions specified in Equation (1). Specifically, we denote by $\mathscr{F}_h^{\mathrm{D}}$ as the portion of the boundary where Dirichlet conditions are imposed and by $\mathscr{F}_h^{\mathrm{N}}$ as the portion where Neumann conditions are set. Additionally, we assume that the triangulation $\mathscr{T}_h$ is constructed in such a way that any face $F \in \mathscr{F}_h$ is entirely contained within either the Dirichlet boundary region, denoted as $\partial\Omega_{\mathrm{D}}$, or the Neumann boundary region, denoted as $\partial\Omega_{\mathrm{N}}$.

We make the assumption that the partition $\mathscr{T}_h$ satisfies the shape regularity conditions outlined in [24, 25]. These conditions ensure the fulfilment of crucial inequalities such as the trace inequality, the inverse inequality, and the approximation property of the L^2-projection on general polygonal/polyhedral meshes. Furthermore, we impose additional regularity assumptions as detailed in [28, 29] to extend the Gagliardo-Nirenberg inequality into a discrete setting.

Assumption 2. *We assume that the sequences of meshes $\{\mathscr{T}_h\}_h$ satisfies the following conditions:*

- *(Shape regularity) for every $K \in \mathscr{T}_h$ and each $h \in (0,1]$ it holds:*

$$h_K^d \lesssim |K| \lesssim h_K^d;$$

- *(Contact regularity) for every $F \in \mathscr{F}_h$ with $F \subset K$ for some $K \in \mathscr{T}_h$ and $h \in (0,1]$ it holds $h_K^{d-1} \lesssim |F|$, where $|F|$ denotes the Hausdorff measure of F;*

- *(Submesh condition) For each $h \in (0,1]$, there exists a shape-regular, conforming, matching simplicial submesh [27] $\widetilde{\mathscr{T}_h}$ such that*

    1. *For each $\widetilde{K} \in \widetilde{\mathscr{T}_h}$ there exists $K \in \mathscr{T}_h$ such that $\widetilde{K} \subseteq K$,*
    2. *The family $\{\widetilde{\mathscr{T}_h}\}_h$ satisfies shape and contact regularity assumptions,*
    3. *for any $\widetilde{K} \in \widetilde{\mathscr{T}_h}$ and any $K \in \mathscr{T}_h$ with $\widetilde{K} \subseteq K$, it holds that $h_K \lesssim h_{\widetilde{K}}$.*

We proceed by defining the functional spaces relevant to our analysis. Considering the time-dependent parabolic problem posed by the continuous formulation in Equation (1), we assume that the solutions belong to the functional space $H^1([0,T], H^1_{\Gamma_{\mathrm{D}}}(\Omega))$. Moreover, we define the Broken Sobolev space $W_q = H^q(\Omega, \mathscr{T}_h) = \{v \in L^2(\Omega) : v|_K \in H^q(K) \, \forall K \in \mathscr{T}_h\}$. We will seek discrete solutions to the problem within the following discontinuous finite element space:

$$W_h^{\mathrm{DG}} = \{w \in L^2(\Omega) : w|_K \in \mathbb{P}_p(K) \, \forall K \in \mathscr{T}_h\},$$

where $\mathbb{P}_p(K)$ is the space of polynomials of total degree $p \geq 1$ defined over the mesh element K.

In conclusion, we recall some notation consistently followed throughout the remainder of the exposition. For vector-valued and tensor-valued functions previous definitions are to be intended as extended componentwise. From now on, all integrals over the domain Ω should be intended as the sum of the contributions over each element K of the partition $\mathscr{T}_h$, in particular, $\|\cdot\| = \left(\sum_{K \in \mathscr{T}_h} \|\cdot\|_{L^2(K)}^2\right)^{1/2}$. Analogously, the L^2-norm on a set of faces $\mathscr{F}_h$ will be indicated as $\|\cdot\|_{\mathscr{F}_h} = (\sum_{F \in \mathscr{F}_h} \|\cdot\|_{L^2(F)}^2)^{1/2}$.

We introduce the following trace-related operators [30]. Each interface $F \in \mathscr{F}_h^{\mathrm{I}}$ is shared by two mesh elements denoted by $K^\pm$, we denote by $\boldsymbol{n}^\pm$ the unit normal vector on face F directed outward with respect to $K^\pm$, respectively. For any sufficiently regular scalar-valued function v and vector-valued function $\boldsymbol{w}$ we set:

- the jump operator $[\![\cdot]\!]$ on $F \in \mathscr{F}_h^{\mathrm{I}}$ as $[\![v]\!] = v^+ \boldsymbol{n}^+ + v^- \boldsymbol{n}^-$ and $[\![\boldsymbol{w}]\!] = \boldsymbol{w}^+ \cdot \boldsymbol{n}^+ + \boldsymbol{w}^- \cdot \boldsymbol{n}^-$,

- the average operator $\{\!\{\cdot\}\!\}$ on $F \in \mathscr{F}_h^{\mathrm{I}}$ as $\{\!\{v\}\!\} = \frac{1}{2}(v^+ + v^-)$ and $\{\!\{\mathbf{w}\}\!\} = \frac{1}{2}(\mathbf{w}^+ + \mathbf{w}^-)$,

where $v^\pm$ and $\boldsymbol{w}^\pm$ denote the traces on F of the function defined over $K^\pm$, respectively. Analogously, we define the jump and average operators on the faces $F \in \mathscr{F}_h^{\mathrm{D}}$, associate with the boundary mesh element K with outward unit normal vector $\boldsymbol{n}$ as:

- the jump operator $[\![\cdot]\!]$ on $F \in \mathscr{F}_h^{\mathrm{D}}$ with Dirichlet condition g and $\boldsymbol{g}$: $[\![v]\!] = (v - g)\boldsymbol{n}$ and $[\![\boldsymbol{w}]\!] = (\boldsymbol{w} - \boldsymbol{g}) \cdot \boldsymbol{n}$;

- the average operator $\{\!\{\cdot\}\!\}$ on $F \in \mathscr{F}_h^{\mathrm{D}}$: $\{\!\{v\}\!\} = v$ and $\{\!\{\boldsymbol{w}\}\!\} = \boldsymbol{w}$.

3.2 PolyDG semi-discrete formulation

In order to derive the semi-discrete formulation of the problem, we introduce the discontinuity penalization function γ_F:

$$\gamma_F = \gamma_0 \begin{cases} \dfrac{p^2}{\{h\}_{\mathrm{H}}}, & \text{on } F \in \mathscr{F}_h^{\mathrm{I}}, \\[2mm] \dfrac{p^2}{h}, & \text{on } F \in \mathscr{F}_h^{\mathrm{D}}, \end{cases} \tag{5}$$

where γ_0 is a constant parameter that should be chosen sufficiently large to ensure the stability of the discrete formulation. We define for any $u_h, w_h, v_h \in W_h^{\mathrm{DG}}$ the following bilinear and trilinear forms:

$$\mathscr{A}(u_h, v_h) = \int_\Omega (\mathbf{D}\nabla_h u_h) \cdot \nabla_h v_h + \sum_{F \in \mathscr{F}_h^{\mathrm{I}} \cup \mathscr{F}_h^{\mathrm{D}}} \int_F \left(\gamma_F [\![u_h]\!] \cdot [\![v_h]\!] - \{\!\{\mathbf{D}\nabla_h u_h\}\!\} \cdot [\![v_h]\!] - [\![u_h]\!] \cdot \{\!\{\mathbf{D}\nabla_h v_h\}\!\} \right), \tag{6a}$$

$$r_N(u_h, w_h, v_h) = \int_\Omega k_{12}\, u_h\, w_h\, v_h, \tag{6b}$$

$$r_L(u_h, v_h) = \int_\Omega k_1\, u_h\, v_h, \tag{6c}$$

$$\widetilde{r}_L(u_h, v_h) = \int_\Omega \widetilde{k}_1\, u_h\, v_h, \tag{6d}$$

$$F_c(v_h) = \int_\Omega f_c\, v_h + \sum_{F \in \mathscr{F}_h^{\mathrm{D}}} \int_F \left(\gamma_F c_{\mathrm{D}h}\, v_h - \mathbf{D}\nabla_h v_h \cdot c_{\mathrm{D}h}\boldsymbol{n} \right), \tag{6e}$$

$$F_q(v_h) = \int_\Omega f_q\, v_h + \sum_{F \in \mathscr{F}_h^{\mathrm{D}}} \int_F \left(\gamma_F q_{\mathrm{D}h}\, v_h - \mathbf{D}\nabla_h v_h \cdot q_{\mathrm{D}h}\boldsymbol{n} \right), \tag{6f}$$

where we denote with $c_{\mathrm{D}h}$ and $q_{\mathrm{D}h}$ suitable approximations of c_{D} and q_{D} in W_h^{DG}, respectively. Moreover, we are using the elementwise gradient $\nabla_h\cdot$ [31]. Finally, the semi-discrete formulation of the problem reads:

Given suitable discrete approximations $c_{0h}, q_{0h} \in W_h^{\mathrm{DG}}$ of the initial conditions of Equation (1), Find $(c_h(t), q_h(t)) \in W_h^{\mathrm{DG}} \times W_h^{\mathrm{DG}}$ for each $t > 0$ such that:

$$\begin{cases} \left(\dfrac{\partial c_h}{\partial t}, w_h \right)_\Omega + \mathscr{A}(c_h, w_h) + r_L(c_h, w_h) + r_N(c_h, q_h, w_h) = F_c(w_h) & \forall w_h \in W_h^{\mathrm{DG}}, \\[4mm] \left(\dfrac{\partial q_h}{\partial t}, v_h \right)_\Omega + \mathscr{A}(q_h, v_h) + \widetilde{r}_L(q_h, v_h) - r_N(q_h, c_h, v_h) = F_q(v_h) & \forall v_h \in W_h^{\mathrm{DG}}. \end{cases} \tag{7}$$

4 Analysis of the semi-discrete PolyDG formulation

This section is dedicated to a detailed analysis of the underlying mathematical properties and conditions that guarantee the problem's well-posedness and will help derive stability and error estimates. Before delving into the main analyses, we present a set of preliminary definitions and recall technical results that are instrumental for the forthcoming analysis. We define the following DG-norms:

$$\|c\|_{\mathrm{DG}} = \left\| \sqrt{\mathbf{D}}\nabla_h c \right\| + \left\| \sqrt{\gamma_F}[\![c]\!] \right\|_{\mathscr{F}_h^{\mathrm{I}} \cup \mathscr{F}_h^{\mathrm{D}}} \quad \forall c \in W_1 \tag{8a}$$

$$\|\!|c|\!\|_{\mathrm{DG}} = \|c\|_{\mathrm{DG}} + \left\| \gamma_F^{-1/2}\{\!\{\mathbf{D}\nabla_h c\}\!\} \right\|_{\mathscr{F}_h^{\mathrm{I}} \cup \mathscr{F}_h^{\mathrm{D}}} \quad \forall c \in W_2. \tag{8b}$$

We recall that the previous norms are equivalent in the space of discontinuous functions W_h^{DG}, under Assumption 2 thanks to the following trace-inverse inequality [24]:

$$\|c\|_{L^2(\partial K)} \lesssim \frac{p^2}{h_K}\|c\|_{L^2(K)} \quad \forall c \in \mathbb{P}_p(K), \quad \forall K \in \mathscr{T}_h. \tag{9}$$

We define also the energy norms:

$$\|c(t)\|_\varepsilon^2 = \|c(t)\|^2 + \int_0^t \|c(s)\|_{\mathrm{DG}}^2 \mathrm{d}s, \tag{10a}$$

$$\|c(t)\|_\varepsilon^2 = \|c(t)\| + \int_0^t \|c(s)\|_{\mathrm{DG}}^2 \mathrm{d}s. \tag{10b}$$

Thus, it can be proven [17] that the bilinear form $\mathscr{A}(\cdot,\cdot)$ is continuous and coercive, namely:

Proposition 1. *Let Assumption 2 be satisfied, then the bilinear form $\mathscr{A}(\cdot,\cdot)$ is such that:*

- $|\mathscr{A}(u_h, v_h)| \lesssim \mathrm{M}\|u_h\|_{\mathrm{DG}}\|v_h\|_{\mathrm{DG}} \quad \forall u_h, v_h \in W_h^{\mathrm{DG}}$;

- $|\mathscr{A}(u, v_h)| \lesssim \widetilde{M}\|u\|_{\mathrm{DG}}\|v_h\|_{\mathrm{DG}} \quad \forall u \in W_2, v_h \in W_h^{\mathrm{DG}}$;

- $\mathscr{A}(u_h, u_h) \gtrsim \mu\|u_h\|_{\mathrm{DG}}^2 \quad \forall u_h \in W_h^{\mathrm{DG}}$;

where M, $\widetilde{M}$ and μ are independent of h. The third bound holds provided that the penalty parameter γ_0 defined in Equation (5) is large enough.

We present two relevant inequalities that play a crucial role in deriving the stability estimate of the discrete solution.

Proposition 2. *(Discrete Gagliardo-Nirenberg inequality) Under Assumption 2, for any $u_h \in W_h^{\mathrm{DG}}$, there exists a constant C_{G_d}, eventually depending on p but independent on h, such that:*

$$\|u_h\|_{L^q(\Omega)} \leq C_{\mathrm{G}_d}\|u_h\|_{\mathrm{DG}}^s \|u_h\|^{1-s}$$

with $s \in (0,1]$ and q satisfying:

$$\frac{1}{q} = s\left(\frac{1}{2} - \frac{1}{d}\right) + \frac{1-s}{2}.$$

The discrete Gagliardo-Nirenberg inequality can be found with complete proof in [29]. For brevity, we present the Petrov inequality without including the proof, which can be found in [32]:

Proposition 3. *Let a, b, c be three positive constants and let $u \in L_+^\infty(0, \hat{t}) = \{u \in L^\infty(0, \hat{t}) : u(t) \geq 0 \text{ a.e. in } (0, \hat{t})\}$ such that:*

$$u(t) \leq a + b\int_0^t u(s)\mathrm{d}s + c\int_0^t u^\eta(s)\mathrm{d}s, \qquad \text{for almost any } t \in (0, \hat{t}), \tag{11}$$

where $\hat{t}$ is such that:

$$e^{b(\eta-1)\hat{t}} < 1 + \frac{b}{a^{\eta-1}c}. \tag{12}$$

Then for almost any $t \in (0, \hat{t})$ we have:

$$u(t) \leq \frac{a\,e^{bt}}{\left(1 - a^{\eta-1}\,c\,b^{-1}\left(e^{b(\eta-1)t} - 1\right)\right)^{\frac{1}{\eta-1}}}. \tag{13}$$

4.1 Stability analysis of the semidiscrete formulation

We can now proceed to derive a stability estimate for the discrete formulation (7).

Theorem 1. *Assume that consider Assumptions 1 and 2 are satisfied, let $(c_h(t), q_h(t)) \in W_h^{DG} \times W_h^{DG}$ be the solution of Problem (7) with $c_D = q_D = 0$ for any $t \in (0, \tilde{t}]$, with $\tilde{t} \leq \mathrm{T}$ introduced in Proposition 3. If the stability parameter γ_0 defined in Equation (5) has been chosen sufficiently large, then:*

$$\|c_h\|_\varepsilon^2 + \|q_h\|_\varepsilon^2 \leq \frac{\left(\|c_{0h}\|^2 + \|q_{0h}\|^2 + \int_0^T \left(\|f_c(s)\|^2 + \|f_q(s)\|^2 \right) ds \right) e^{\beta t}}{\left(\widetilde{\mu}^{d-1} - \xi \left(\|c_{0h}\|^2 + \|q_{0h}\|^2 + \int_0^T \left(\|f_c(s)\|^2 + \|f_q(s)\|^2 \right) \right)^{d-1} \left(e^{\beta(d-1)t} - 1 \right) \right)^{\frac{1}{d-1}}} \tag{14}$$

where:

$$\widetilde{\mu} = \min\{1, \mu\} \qquad \beta = \frac{1}{\widetilde{\mu}} \left(2 \max\left\{ K_1, \widetilde{K}_1 \right\} + 1 \right) \qquad \xi = \frac{\mathrm{C}_{\mathrm{G}_d}^3 K_{12}^2}{2^{d-2} \mu \left(2 \max\left\{ \mathrm{K}_1, \widetilde{\mathrm{K}}_1 \right\} + 1 \right)}$$

having defined $K_{12} = \|k_{12}\|_{L^\infty}$, $K_1 = \|k_1\|_{L^\infty}$, $\widetilde{K}_1 = \|\tilde{k}_1\|_{L^\infty}$, and $\mathrm{C}_{\mathrm{G}_d}$ from Proposition 2.

Proof. We sum the two equations in (7) and we introduce the notation $\dot{u} = \frac{\partial u}{\partial t}$ for each $u \in W_h^{\mathrm{DG}}$:

$$(\dot{c}_h, w_h)_\Omega + (\dot{q}_h, v_h)_\Omega + \mathscr{A}(c_h, w_h) + \mathscr{A}(q_h, v_h) = \\ -r_L(c_h, w_h) - \widetilde{r}_L(q_h, v_h) - r_N(c_h, q_h, w_h) + r_N(q_h, c_h, v_h) + F_c(w_h) + F_q(v_h). \tag{15}$$

By choosing as trial functions $w_h = c_h(t)$ and $v_h = q_h(t)$, we integrate in time Equation (15) and exploit Proposition 1 to get:

$$\frac{1}{2}\|c_h(t)\|^2 - \frac{1}{2}\|c_{0h}\|^2 + \int_0^t \mu\|c_h(s)\|_{\mathrm{DG}}^2 \, ds + \frac{1}{2}\|q_h(t)\|^2 - \frac{1}{2}\|q_{0h}\|^2 + \int_0^t \mu\|q_h(s)\|_{\mathrm{DG}}^2 \, ds \leq \\ -r_L(c_h(t), c_h(t)) - \widetilde{r}_L(q_h(t), q_h(t)) - r_N(c_h(t), q_h(t), c_h(t)) + r_N(q_h(t), c_h(t), q_h(t)) + F_c(c_h(t)) + F_q(q_h(t)).$$

On the other hand, thanks to coefficients regularity (1) and Hölder's and Young's inequalities, we obtain:

$$\frac{1}{2}\|c_h(t)\|^2 - \frac{1}{2}\|c_{0h}\|^2 + \int_0^t \mu\|c_h(s)\|_{\mathrm{DG}}^2 \, ds + \frac{1}{2}\|q_h(t)\|^2 - \frac{1}{2}\|q_{0h}\|^2 + \int_0^t \mu\|q_h(s)\|_{\mathrm{DG}}^2 \, ds \leq \\ + \frac{1 + 2K_1}{2} \int_0^t \|c_h(s)\|^2 ds + \frac{1 + 2\widetilde{K}_1}{2} \int_0^t \|q_h(s)\|^2 ds + \frac{1}{2} \int_0^t \|f_c(s)\|^2 ds + \frac{1}{2} \int_0^t \|f_q(s)\|^2 ds \\ + \int_0^t |r_N(c_h(s), q_h(s), c_h(s)) + r_N(q_h(s), c_h(s), q_h(s))| ds,$$

where $K_1 = \|k_1\|_{L^\infty(\Omega)}$ and $\widetilde{K}_1 = \|\tilde{k}_1\|_{L^\infty(\Omega)}$. Concerning the non-linear terms we apply first the Hölder's inequality to obtain:

$$\int_0^t |r_N(c_h(s), q_h(s), c_h(s)) + r_N(q_h(s), c_h(s), q_h(s))| ds \leq K_{12} \int_0^t \left(\int_\Omega |c_h^2(s) q_h(s)| + |q_h^2(s) c_h(s)| \right) ds,$$

where $K_{12} = \|k_{12}\|_{L^\infty(\Omega)}$. Then we employ Hölder's inequality with $\gamma = 3/2$ and $\gamma' = 3$ on each term and get:

$$\int_\Omega \left(|c_h^2 q_h| + |c_h q_h^2| \right) \leq \left(\int_\Omega c_h^3 \right)^{2/3} \left(\int_\Omega q_h^3 \right)^{1/3} + \left(\int_\Omega c_h^3 \right)^{1/3} \left(\int_\Omega q_h^3 \right)^{2/3} \leq \|c_h\|_{L^3}^2 \|q_h\|_{L^3} + \|c_h\|_{L^3} \|q_h\|_{L^3}^2.$$

Subsequently we apply the Young's inequality with exponents $\alpha = 3/2$ and $\beta = 3$ and then sum up the two contributions:

$$\int_0^t |r_N(c_h(s), q_h(s), c_h(s)) + r_N(q_h(s), c_h(s), q_h(s))| ds \leq K_{12} \int_0^t \left(\|c_h(s)\|_{L^3}^3 + \|q_h(s)\|_{L^3}^3 \right) ds.$$

In order to exploit the Gagliardo-Nirenberg inequality in Proposition 2, we distinguish 2 cases:

8

- $d = 2$, then $s = 1/3$ and the Young's inequality can be applied with exponents $\alpha = \beta = 2$ and with an $\epsilon > 0$:

$$\|c_h\|_{L^3}^3 \leq \frac{C_{G_d}^3}{2} \left(\epsilon \|c_h\|_{DG}^2 + \frac{1}{\epsilon} \|c_h\|^4 \right);$$

- $d = 3$, then $s = 1/2$ and Young's inequality can be applied with exponents $\alpha = 4/3$, $\beta = 4$ and with an $\epsilon > 0$:

$$\|c_h\|_{L^3}^3 \leq \frac{C_{G_d}^3}{4} \left(3\epsilon \|c_h\|_{DG}^2 + \frac{1}{\epsilon} \|c_h\|^6 \right).$$

Then by choosing $\epsilon = 2\mu/(dK_{12}C_{G_d}^3)$, we obtain:

$$
\|c_h(t)\|^2 + \|q_h(t)\|^2 + \mu \int_0^t \left(\|c_h(s)\|_{DG}^2 + \|q_h(s)\|_{DG}^2 \right) \mathrm{d}s \leq \|c_{0h}\|^2 + \|q_{0h}\|^2 + \int_0^T \left(\|f_c(s)\|^2 + \|f_q(s)\|^2 \right) \mathrm{d}s
$$
$$
+ \left(2 \max\left\{ K_1, \widetilde{K}_1 \right\} + 1 \right) \int_0^t \left(\|c_h(s)\|^2 + \|q_h(s)\|^2 \right) \mathrm{d}s + \frac{dK_{12}^2 C_{G_d}^6}{2^{d-3}\mu} \int_0^t \left(\|c_h(s)\|^{2d} + \|q_h(s)\|^{2d} \right) \mathrm{d}s.
\tag{16}
$$

Finally, we can define a positive constant $\widetilde{\mu} = \min\{1, \mu\}$ and by applying Perov's inequality in Proposition 3, we deduce the thesis. $\square$

Remark 1. *Under the assumptions of Theorem 1, if $f_c = f_q = 0$, estimate (14) reduces to:*

$$\|c_h\|_\epsilon^2 + \|q_h\|_\epsilon^2 \lesssim \frac{\left(\|c_{0h}\|^2 + \|q_{0h}\|^2 \right) e^{\beta t}}{\left(\widetilde{\mu}^{d-1} - \xi \left(\|c_{0h}\|^2 + \|q_{0h}\|^2 \right)^{d-1} \left(e^{\beta(d-1)t} - 1 \right) \right)^{\frac{1}{d-1}}} = C_S \tag{17}$$

4.2 Error analysis of the semidiscrete formulation

Theorem 2. *Let problem (1) with $f_c = f_q = 0$ and $c_D = q_D = 0$. Let the couple of functions $(c(t), q(t))$ be the solution of Problem (1) for any $t \in (0, T]$ and let them satisfy the additional regularity requirements:*

$$c, q \in C^1([0, T], H^n(\Omega)), \quad \text{with } n \geq 2.$$

Under Assumptions 1 and 2, let $(c_h(t), q_h(t))$ be the solution of (7), for a sufficiently large penalty parameter γ_0. Then, the following estimate holds:

$$
\|c(t) - c_h(t)\|_\varepsilon^2 + \|q(t) - q_h(t)\|_\varepsilon^2 \lesssim \sum_{K \in \mathscr{T}_h} h_K^{2\min(p+1,n)-2} \Big(\|c(t)\|_{H^n(K)}^2 + \|q(t)\|_{H^n(K)}^2
$$
$$
+ \int_0^t \left(\|c(s)\|_{H^n(K)}^2 + \|\dot{c}(s)\|_{H^n(K)}^2 + \|q(s)\|_{H^n(K)}^2 + \|\dot{q}(s)\|_{H^n(K)}^2 \right) \mathrm{d}s \Big),
$$

provided that the constants fulfil the following relations:

$$2\mu - (K_{12}C_I + Q_I + 2K_1) C_{E_2}^2 - 2K_{12}C_S C_{E_4}^2 > 0 \qquad 2\mu - \left(K_{12}C_I + Q_I + 2\widetilde{K}_1 \right) C_{E_2}^2 - 2K_{12}C_S C_{E_4}^2 > 0,$$

where μ and $\widetilde{M}$ are defined as in Proposition 1, $K_{12} = \|k_{12}\|_{L^\infty}$, C_S is defined as in Equation (17) and C_{E_q} is the discrete Sobolev embedding constant for the $L^q(\Omega)$-space [27].

Proof. Let us consider the weak solution of the heterodimer model (c, q), then due to the consistency of the DG formulation, it holds:

$$(\dot{c}, w_h)_\Omega + (\dot{q}, v_h)_\Omega + \mathscr{A}(c, w_h) + \mathscr{A}(q, v_h) = -r_L(c, w_h) - \widetilde{r}_L(q, v_h) - r_N(c, q, w_h) + r_N(q, c, v_h). \tag{18}$$

We subtract Equations (15) and (18) and consider the interpolant of the exact solutions $c_I, q_I \in W_h^{DG}$ [33], respectively, then rewrite the errors as:

$$c - c_h = (c - c_I) + (c_I - c_h) = e_I^c + e_h^c, \qquad q - q_h = (q - q_I) + (q_I - q_h) = e_I^q + e_h^q.$$

We test the obtained formulation with respect to $w_h = e_h^c$ and $v_h = e_h^q$ and integrate along the time interval $[0, t]$:

$$\int_0^t \left((\dot{e}_h^c(s), e_h^c(s))_\Omega + (\dot{e}_h^q(s), e_h^q(s))_\Omega + \mathscr{A}(e_h^c(s), e_h^c(s)) + \mathscr{A}(e_h^q(s), e_h^q(s)) \right) \mathrm{d}s = \int_0^t \Big(-r_L(e_h^c(s), e_h^c(s))$$

$$-\widetilde{r}_L(e_h^q(s), e_h^q(s)) - r_N(c(s), q(s), e_h^c(s)) + r_N(c_h(s), q_h(s), e_h^c(s)) + r_N(q(s), c(s), e_h^q(s)) - r_N(q_h(s), c_h(s), e_h^q(s))$$

$$-(\dot{e}_I^c(s), e_h^c(s))_\Omega - (\dot{e}_I^q(s), e_h^q(s))_\Omega - \mathscr{A}(e_I^c(s), e_h^c(s)) - \mathscr{A}(e_I^q(s), e_h^q(s)) - r_L(e_I^c(s), e_h^c(s)) - \widetilde{r}_L(e_I^q(s), e_h^q(s)) \Big) \mathrm{d}s.$$

We proceed by exploiting the coercivity and continuity of the bilinear form $\mathscr{A}$ in Proposition 1, and by means of Hölder's and Young's inequalities:

$$\frac{1}{2}\|e_h^c(t)\|^2 + \frac{1}{2}\|e_h^q(t)\|^2 + \int_0^t \mu \left(\|e_h^c(s)\|_{\mathrm{DG}}^2 + \|e_h^q(s)\|_{\mathrm{DG}}^2 \right) \mathrm{d}s \leq + \int_0^t \left(K_1 \|e_h^c(s)\|^2 + \widetilde{K}_1 \|e_h^q(s)\|^2 \right) \mathrm{d}s$$

$$+ K_{12} \int_0^t \left(|(c(s)q(s) - c_h(s)q_h(s), e_h^c(s))_\Omega| + |(c(s)q(s) - c_h(s)q_h(s), e_h^q(s))_\Omega| \right) \mathrm{d}s$$

$$+ \int_0^t \left((\|\dot{e}_I^c(s)\| + K_1\|e_I^c(s)\|) \|e_h^c(s)\| + \left(\|\dot{e}_I^q(s)\| + \widetilde{K}_1\|e_I^q(s)\| \right) \|e_h^q(s)\| \right) \mathrm{d}s$$

$$+ \int_0^t \left(\widetilde{M}\|e_I^c(s)\|_{\mathrm{DG}} \|e_h^c(s)\|_{\mathrm{DG}} + \widetilde{M}\|e_I^q(s)\|_{\mathrm{DG}} \|e_h^q(s)\|_{\mathrm{DG}} \right) \mathrm{d}s.$$

Concerning the nonlinear term, we observe that:

$$cq - c_h q_h = cq - qc_I + qc_I - q_h c_I + q_h c_I - q_h c_h$$

$$= q \underbrace{(c - c_I)}_{e_I^c} + c_I \underbrace{(q - q_h)}_{e_I^q + e_h^q} + q_h \underbrace{(c_I - c_h)}_{e_h^c}.$$

Therefore:

$$|(cq - c_h q_h, e_h^c)_\Omega| = \underbrace{|(qe_I^c, e_h^c)_\Omega|}_{(\mathrm{I})} + \underbrace{|(c_I e_I^q, e_h^c)_\Omega|}_{(\mathrm{II})} + \underbrace{|(c_I e_h^q, e_h^c)_\Omega|}_{(\mathrm{III})} + \underbrace{|(q_h e_h^c, e_h^c)_\Omega|}_{(\mathrm{IV})}.$$

The terms on the right-hand side above can be treated separately as follows:

(I) Using that the exact solution $q(t) \in L^\infty(\Omega)$ for any $t > 0$, Hölder's and Young's inequalities to obtain:

$$|(q\, e_I^c, e_h^c)_\Omega| \leq \|q\|_{L^\infty((0,T];L^\infty(\Omega))} \|e_I^c\| \|e_h^c\| =: Q\|e_I^c\| \|e_h^c\|;$$

(II) Using that the interpolant is bounded by construction $c_I(t) \in L^\infty(\Omega)$ for any $t > 0$, Hölder's and Young's inequality leads to:

$$|(c_I\, e_I^q, e_h^c)_\Omega| \leq \|c_I\|_{L^\infty((0,T];L^\infty(\Omega))} \|e_I^q\| \|e_h^c\| =: C_I\|e_I^q\| \|e_h^c\|;$$

(III) We exploit the interpolant boundedness, Hölder's, Young's, and Sobolev-Poincarè-Wirtinger discrete inequality [27] to achieve:

$$|(c_I\, e_h^q, e_h^c)_\Omega| \leq \frac{C_I}{2} \left(\|e_h^q\|^2 + \|e_h^c\|^2 \right) \leq \frac{C_I C_{E_2}^2}{2} \left(\|e_h^q\|_{\mathrm{DG}}^2 + \|e_h^c\|_{\mathrm{DG}}^2 \right);$$

(IV) We exploit the stability estimate and Sobolev-Poincarè-Wirtinger discrete inequality [27] that leads to:

$$|(q_h\, e_h^c, e_h^c)_\Omega| \leq C_S\|e_h^c\|_{L^4(\Omega)}^2 \leq C_S C_{E_4}^2 \|e_h^c\|_{\mathrm{DG}}^2;$$

Analogous considerations can be done to treat the second nonlinear term, by defining $C = \|c\|_{L^\infty((0,T];L^\infty(\Omega))}$ and $Q_I = \|q_I\|_{L^\infty((0,T];L^\infty(\Omega))}$. Taking into account all previous bounds and by using Sobolev-Poincarè-Wirtinger discrete

10

inequality as in [27] we get:

$$
\frac{1}{2}\|e_h^c(t)\|^2 + \frac{1}{2}\|e_h^q(t)\|^2 + \int_0^t \left(\mu - \left(K_{12}\frac{C_{\mathrm{I}}+Q_{\mathrm{I}}}{2} + K_1\right)C_{E_2}^2 - K_{12}C_S C_{E_4}^2\right)\|e_h^c(s)\|_{\mathrm{DG}}^2 \mathrm{d}s
$$

$$
+ \int_0^t \left(\mu - \left(K_{12}\frac{C_{\mathrm{I}}+Q_{\mathrm{I}}}{2} + \widetilde{K}_1\right)C_{E_2}^2 - K_{12}C_S C_{E_4}^2\right)\|e_h^q(s)\|_{\mathrm{DG}}^2 \mathrm{d}s \le
$$

$$
+ \int_0^t \left(\|\dot{e}_{\mathrm{I}}^c(s)\| + (K_1 + K_{12}Q)\|e_{\mathrm{I}}^c(s)\| + K_{12}C_{\mathrm{I}}\|e_{\mathrm{I}}^q(s)\|\right)\|e_h^c(s)\|\mathrm{d}s
$$

$$
+ \int_0^t \left(\|\dot{e}_{\mathrm{I}}^q(s)\| + (\widetilde{K}_1 + K_{12}C)\|e_{\mathrm{I}}^q(s)\| + K_{12}Q_{\mathrm{I}}\|e_{\mathrm{I}}^c(s)\|\right)\|e_h^q(s)\|\mathrm{d}s
$$

$$
+ \int_0^t \left(\widetilde{M}\|e_{\mathrm{I}}^c(s)\|_{\mathrm{DG}}\|e_h^c(s)\|_{\mathrm{DG}} + \widetilde{M}\|e_{\mathrm{I}}^q(s)\|_{\mathrm{DG}}\|e_h^q(s)\|_{\mathrm{DG}}\right)\mathrm{d}s.
$$

Considering the relation between the DG-norms, we obtain that if $2\mu - (K_{12}C_{\mathrm{I}} + Q_{\mathrm{I}} + 2K_1)C_{E_2}^2 - 2K_{12}C_S C_{E_4}^2 > 0$ and $2\mu - \left(K_{12}C_{\mathrm{I}} + Q_{\mathrm{I}} + 2\widetilde{K}_1\right)C_{E_2}^2 - 2K_{12}C_S C_{E_4}^2 > 0$ we can ensure the positivity of the coefficients in the left-hand side and adopt the notation $\lesssim$ from now on, i.e.,

$$
\|e_h^c(t)\|_\varepsilon^2 + \|e_h^q(t)\|_\varepsilon^2 \lesssim \int_0^t \left(\|\dot{e}_{\mathrm{I}}^c(s)\| + \|e_{\mathrm{I}}^c(s)\| + \|e_{\mathrm{I}}^q(s)\|\right)\|e_h^c(s)\|\mathrm{d}s
$$

$$
+ \int_0^t \left(\|\dot{e}_{\mathrm{I}}^q(s)\| + \|e_{\mathrm{I}}^q(s)\| + \|e_{\mathrm{I}}^c(s)\|\right)\|e_h^q(s)\|\mathrm{d}s + \int_0^t \left(\|e_{\mathrm{I}}^c(s)\|_{\mathrm{DG}}\|e_h^c(s)\|_{\mathrm{DG}} + \|e_{\mathrm{I}}^q(s)\|_{\mathrm{DG}}\|e_h^q(s)\|_{\mathrm{DG}}\right)\mathrm{d}s.
$$

By application of Hölder's inequality and Grönwall's lemma [31] we get:

$$
\|e_h^c(t)\|_\varepsilon^2 + \|e_h^q(t)\|_\varepsilon^2 \lesssim \int_0^t \left(\|\dot{e}_{\mathrm{I}}^c(s)\|^2 + \|e_{\mathrm{I}}^c(s)\|^2 + \|e_{\mathrm{I}}^c(s)\|_{\mathrm{DG}}^2 + \|\dot{e}_{\mathrm{I}}^q(s)\|^2 + \|e_{\mathrm{I}}^q(s)\|^2 + \|e_{\mathrm{I}}^c(s)\|_{\mathrm{DG}}^2\right)\mathrm{d}s.
$$

We can bound each term with the interpolation error estimate [34]:

$$
\|e_h^c\|_\varepsilon^2 + \|e_h^q\|_\varepsilon^2 \lesssim \sum_{K\in\mathscr{T}_h} h_L^{2\min(p+1,n)-2}\int_0^t \left(\|c(s)\|_{\mathrm{H}^n(\mathrm{K})}^2 + \|\dot{c}(s)\|_{\mathrm{H}^n(\mathrm{K})}^2 + \|q(s)\|_{\mathrm{H}^n(\mathrm{K})}^2 + \|\dot{q}(s)\|_{\mathrm{H}^n(\mathrm{K})}^2\right).
$$

Finally, by application of the triangular inequality:

$$
\|c - c_h\|_\varepsilon^2 + \|q - q_h\|_\varepsilon^2 \le \|e_h^c\|_\varepsilon^2 + \|e_{\mathrm{I}}^c\|_\varepsilon^2 + \|e_h^q\|_\varepsilon^2 + \|e_{\mathrm{I}}^q\|_\varepsilon^2,
$$

and taking into account the interpolation error estimate, the thesis follows. $\qquad\square$

Remark 2. *If the grid is quasi-uniform and the exact solutions $c(t), q(t) \in H^p(\Omega)$ for all $t \in (0, T]$, where p is the polynomial approximation degree in any $K \in \mathscr{T}_h$ then Theorem 2 reduces to:*

$$
\|c(t) - c_h(t)\|_\varepsilon^2 + \|q(t) - q_h(t)\|_\varepsilon^2 \sim O(h^p). \tag{19}
$$

5 Fully discrete formulation

In this section, we present the fully discrete formulation of Problem (7) in its algebraic form.

5.1 Algebraic formulation of the semidiscrete problem

We consider $\{\phi_j\}_{j=0}^{N_h}$ a set of basis function for W_h^{DG}, being N_h its dimension. We can write the discrete solutions expansion with respect to the chosen base, i.e. $c_h(\boldsymbol{x}, t) = \sum_{j=0}^{N_h} \mathbf{C}_j(t)\phi_j(\boldsymbol{x})$ and $q_h(\boldsymbol{x}, t) = \sum_{j=0}^{N_h} \mathbf{Q}_j(t)\phi_j(\boldsymbol{x})$. We denote by $\mathbf{C}, \mathbf{Q} \in \mathbb{R}^{N_h}$, the corresponding expansion coefficients vectors. We also define the following matrices

$$
\begin{aligned}
[\mathrm{M}]_{i,j} &= (\phi_j, \phi_i)_\Omega & &\text{Mass matrix} \\
[\mathrm{A}]_{i,j} &= \mathscr{A}(\phi_j, \phi_i) & &\text{Stiffness matrix} \\
[\mathrm{R}_N(\Phi(t))]_{i,j} &= r_N(\Phi_h(t), \phi_j, \phi_i) & &\mathrm{Non-linear\ reaction\ matrix} \\
[\mathrm{R}_L]_{i,j} &= r_L(\phi_j, \phi_i) & &\text{Linear reaction matrix} \\
[\widetilde{\mathrm{R}}_L]_{i,j} &= \widetilde{r}_L(\phi_j, \phi_i) & &\text{Linear reaction matrix}
\end{aligned}
$$

with $i, j = 1, ..., N_h$. Moreover, we introduce the right-hand side vectors : $[\mathbf{F}_c]_i = F_c(\phi_i)$ and $[\mathbf{F}_q]_i = F_q(\phi_i)$ with $i = 1, ..., N_h$. We then rewrite the problem (7) in algebraic form:

$$
\begin{cases}
\mathrm{M}\dot{\mathbf{C}}(t) + \mathrm{A}\mathbf{C}(t) + \mathrm{R}_L\mathbf{C}(t) + \mathrm{R}_N(\mathbf{C}(t))\mathbf{Q}(t) = \mathbf{F}_c(t) & t \in (0, T] \\[4pt]
\mathrm{M}\dot{\mathbf{Q}}(t) + \mathrm{A}\mathbf{Q}(t) + \widetilde{\mathrm{R}}_L\mathbf{Q}(t) - \mathrm{R}_N(\mathbf{Q}(t))\mathbf{C}(t) = \mathbf{F}_q(t) & t \in (0, T] \\[4pt]
\mathbf{C}(0) = \mathbf{C}_0, \ \ \mathbf{Q}(0) = \mathbf{Q}_0.
\end{cases}
\tag{20}
$$

5.2 Time discretization

We construct a partition $0 < t_1 < t_2 < ... < t_{N_T} = T$ of the time interval $[0, T]$ into N_T intervals of constant time step $\Delta t = t_{n+1} - t_n$. We denote with $\mathbf{C}^n \simeq \mathbf{C}(t_n)$. We assemble the fully discrete approximation of Problem (20) by means of the ϑ-method, depending upon the user-set parameter $\vartheta \in [0, 1]$.

Given the initial conditions vectors $\mathbf{C}^0 = \mathbf{C}(0)$ and $\mathbf{Q}^0 = \mathbf{Q}(0)$, for $n = 1, ..., N_T$ find $(\mathbf{C}^n, \mathbf{Q}^n)$ solution of the following system of equations:

$$
\begin{cases}
\left(\dfrac{\mathrm{M}}{\Delta t} + \vartheta\mathrm{A} + \vartheta\mathrm{R}_L\right)\mathbf{C}^n + \mathrm{R}_N(\mathbf{C}^*)\mathbf{Q}^{n,n-1} = \mathbf{F}_c^n, \\[10pt]
\left(\dfrac{\mathrm{M}}{\Delta t} + \vartheta\mathrm{A} + \vartheta\widetilde{\mathrm{R}}_L\right)\mathbf{Q}^n - \mathrm{R}_N(\mathbf{Q}^*)\mathbf{C}^{n,n-1} = \mathbf{F}_q^n,
\end{cases}
\tag{21}
$$

where:

$$
\mathbf{F}_c^n = \vartheta\mathbf{F}_c(t_n) + (1 - \vartheta)\mathbf{F}_c(t_{n-1}) + \frac{M}{\Delta t}\mathbf{C}^{n-1} - (1 - \vartheta)(\mathrm{A} + \mathrm{R}_L)\mathbf{C}^{n-1},
$$

$$
\mathbf{F}_q^n = \vartheta\mathbf{F}_q(t_n) + (1 - \vartheta)\mathbf{F}_q(t_{n-1}) + \frac{M}{\Delta t}\mathbf{Q}^{n-1} - (1 - \vartheta)(\mathrm{A} + \widetilde{\mathrm{R}}_L)\mathbf{Q}^{n-1}.
$$

We denoted with $\mathbf{C}^*$ and $\mathbf{Q}^*$ the approximation of $\mathbf{C}^n$ and $\mathbf{Q}^n$, chosen to linearize the system (21). In practive we will consider the following options:

- Implicit Euler method ($\vartheta = 1$):
$$
\mathrm{R}_N(\mathbf{Q}^*)\mathbf{C}^{n,n-1} = \mathbf{Q}^{n-1}\,\mathbf{C}^n;
$$

- Crank-Nicolson method ($\vartheta = 1/2$):
$$
\mathrm{R}_N(\mathbf{Q}^*)\mathbf{C}^{n,n-1} = \left(\frac{3}{2}\mathbf{Q}^{n-1} - \frac{1}{2}\mathbf{Q}^{n-2}\right)\frac{1}{2}\left(\mathbf{C}^n + \mathbf{C}^{n-1}\right).
$$

6 Numerical results: verification

In this section, we provide a comprehensive exposition of the results derived from the numerical test performed in order to assess the accuracy of the method, validate the error estimate introduced in Section 2, and analyze the traveling-wave solution behavior. The numerical simulations are based on the Lymph library [35], implementing the PolyDG method. Moreover, for all the subsequent tests, we set the penalty parameter $\gamma_0 = 10$.

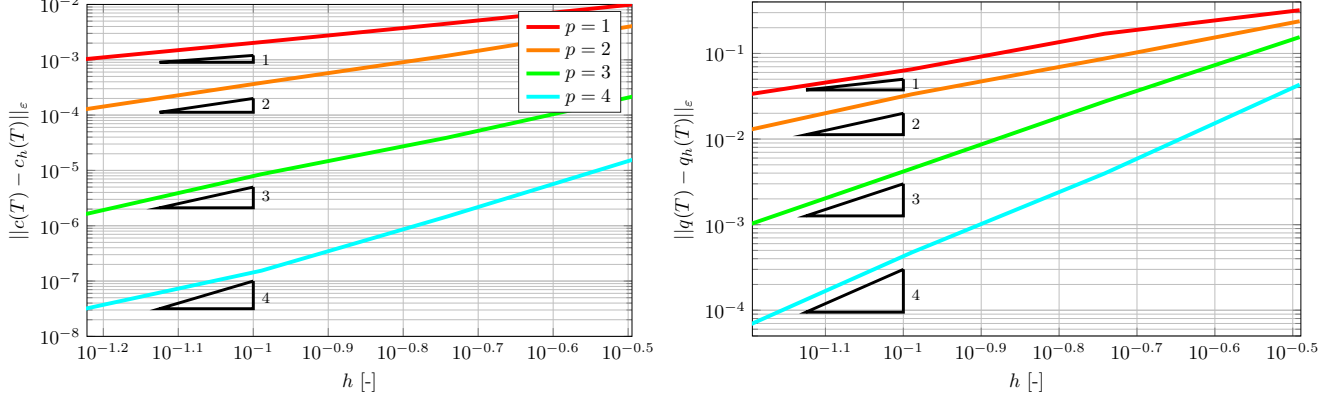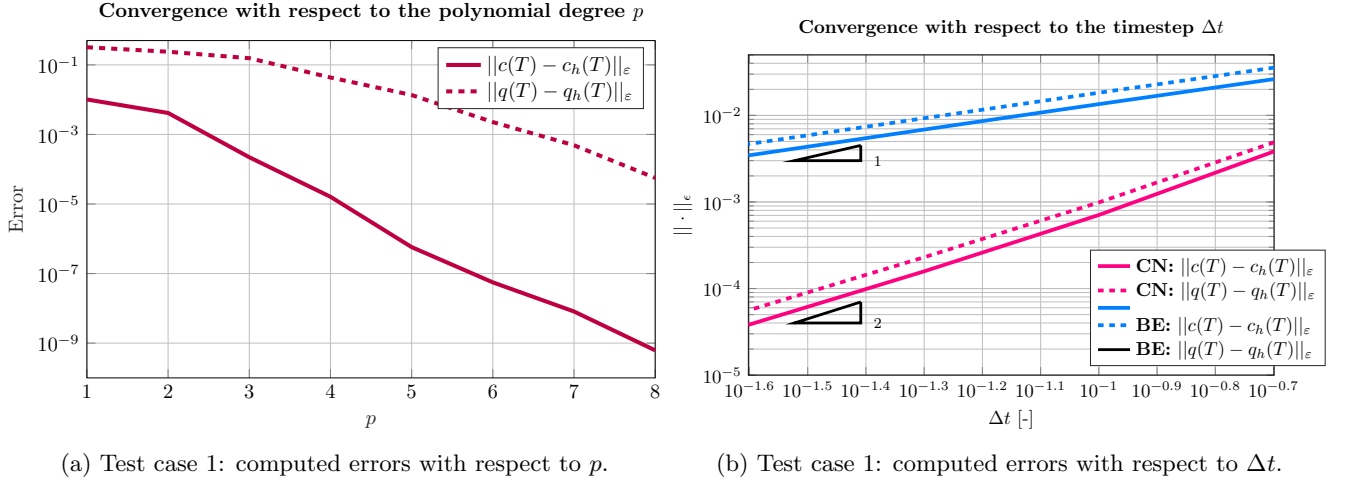| Parameter	Value		Parameter	Value	
d_{ext}	1.00	[mm^2/years]	d_{axn}	0.00	[mm^2/years]
k_0	0.00	[1/years]	k_{12}	1.00	[1/years]
k_1	1.00	[1/years]	$\tilde{k}_1$	1.00	[1/years]

Table 1: Physical parameter values used in Test 1 and Test 2.

Figure 2: Test case 1: computed errors and computed convergence rates versus h for different choices of the polynomial degree $p = 1, 2, 3, 4$ and for the solutions c_h (left) and q_h (right).

(a) Test case 1: computed errors with respect to p.

(b) Test case 1: computed errors with respect to Δt.

Figure 3: Test case 1: computed errors and convergence rates with respect to p (left) and Δt (right). The results on the left panel have been obtained with the Crank-Nicolson (CN) time integration scheme; the results on the right panel have been obtained with both Backward Euler (BE) and CN schemes.

6.1 Test 1: convergence analysis

We consider the domain $\Omega = (0,1)^2$ discretized into a polygonal mesh generated by PolyMesher [36]. In the current phase of the study, we are focused on examining isotropic diffusion and for the model parameters we adopt the values summarized in Table 1. We establish a predefined exact solution as:

$$c(x, y, t) = (\cos(\pi x) + \cos(\pi y)) \cos(t),$$
$$q(x, y, t) = (\cos(4\pi x) \cos(4\pi y) + 2)e^{-t}.$$

The forcing terms denoted as f_c and f_q, and the Dirichlet boundary conditions represented as c_{D} and q_{D} are chosen accordingly.

In Figure 2 we report the numerical results of the convergence test performed with respect to the mesh size parameter h. We use a time discretization step $\Delta t = 10^{-5}$ and fix a final time instant $T = 10^{-3}$. We collect
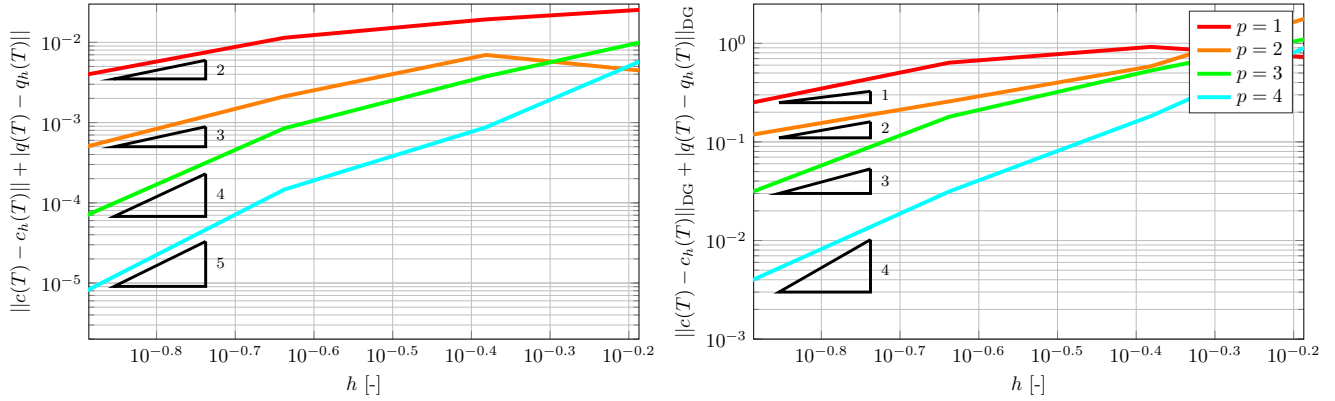
13

Figure 4: Test case 2: computed errors and computed convergence rates versus h for different choices of the polynomial degree $p = 1, 2, 3, 4$ and for the solutions c_h (left) and q_h (right).

Method		$p = 1$			$p = 2$	
h	**DOFs**	$T_1 = 5$	$T_2 = 10$	**DOFs**	$T_1 = 5$	$T_2 = 10$
0.736	90	4.62×10^{-2}	4.62×10^{-2}	180	2.74×10^{-2}	2.67×10^{-2}
0.415	300	2.83×10^{-2}	2.74×10^{-2}	600	8.79×10^{-3}	9.38×10^{-3}
0.230	900	1.55×10^{-2}	1.76×10^{-2}	1800	2.33×10^{-3}	2.78×10^{-3}
0.129	3000	6.24×10^{-3}	5.65×10^{-3}	6000	4.63×10^{-4}	4.39×10^{-4}

Method		$p = 3$			$p = 4$	
h	**DOFs**	$T_1 = 5$	$T_2 = 10$	**DOFs**	$T_1 = 5$	$T_2 = 10$
0.736	300	8.09×10^{-3}	9.07×10^{-3}	450	8.19×10^{-3}	7.78×10^{-3}
0.415	1000	3.22×10^{-3}	2.77×10^{-3}	1500	1.21×10^{-3}	1.19×10^{-3}
0.230	3000	5.29×10^{-4}	5.31×10^{-4}	4500	1.29×10^{-4}	2.05×10^{-4}
0.129	10000	4.99×10^{-5}	4.77×10^{-5}	15000	5.71×10^{-6}	5.29×10^{-6}

Table 2: Computed errors with L^2-norm of the error of $\|q(T) - q_h(T)\|$ at different final time instants (errors for c_h are analogous).

the energy norm of the error as defined in Equation (10a) for each solution and repeat the test keeping fixed the polynomial degree of approximation $p = 1, 2, 3, 4$, while progressively refining the mesh ($N_{el} = 30, 100, 300, 1000$, where N_{el} denotes the number of polygons of the domain partition). We can observe that the optimal rate of convergence is always achieved as expected from theory.

In Figure 3a we report the energy norm of the error with respect the polynomial degree p. We repeat the numerical tests keeping fixed the polygonal mesh characterized by $N_{el} = 30$ and the time discretization $\Delta t = 10^{-5}$ while considering an increasing polynomial order $p = 1, ..., 8$. Even if the dependency of the energy norm of the error from p has not been covered by the theoretical analysis performed in Section 4 we numerically demonstrated that exponential convergence is obtained.

Finally, a convergence test with respect to the time discretization step Δt has been reported in Figure 3b. The test set the most refined polygonal mesh with $N_{el} = 1000$ and $p = 6$, and we registered the error in energy norm obtained for different time steps $\Delta t = 0.2, 0.1, 0.05, 0.025$. We compare the Backward Euler and Crank-Nicolson methods. We can observe that the Backward Euler method (characterized by setting $\theta = 1$) exhibits theoretical linear convergence with respect to Δt, whereas the error decays with a second-order rate for Crank-Nicolson method ($\theta = 0.5$).

6.2 Test 2: simulation of a travelling wave

The objective of this test is to evaluate the method's ability to accurately replicate the dynamics of a travelling-wave solution as it drives the system towards the unstable equilibrium state. To accomplish this we consider a rectangular domain $\Omega = (0, 5) \times (0, 1)$ partitioned via Polymesher [36]. We impose as the exact solution a couple of
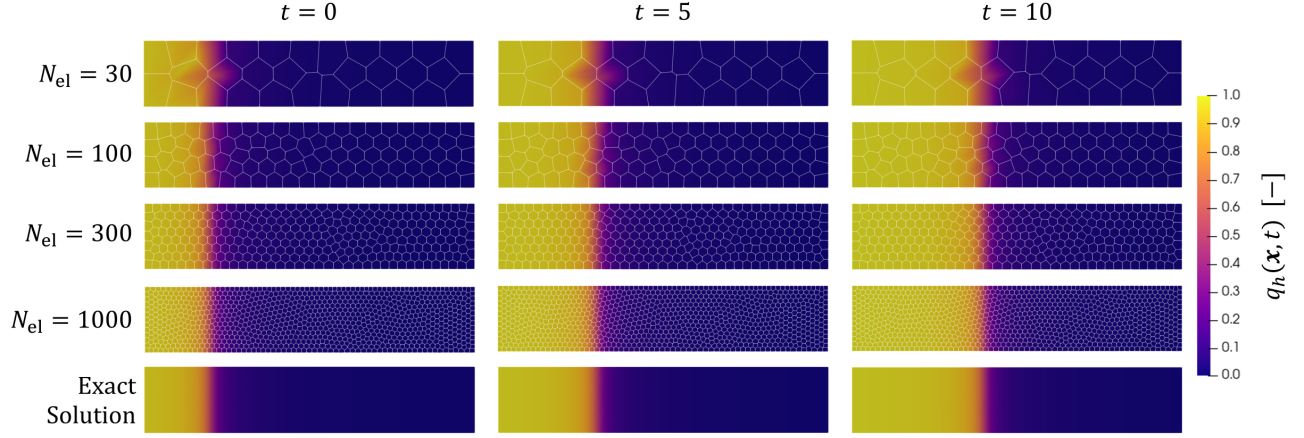
(a) Wavefront propagation of q.
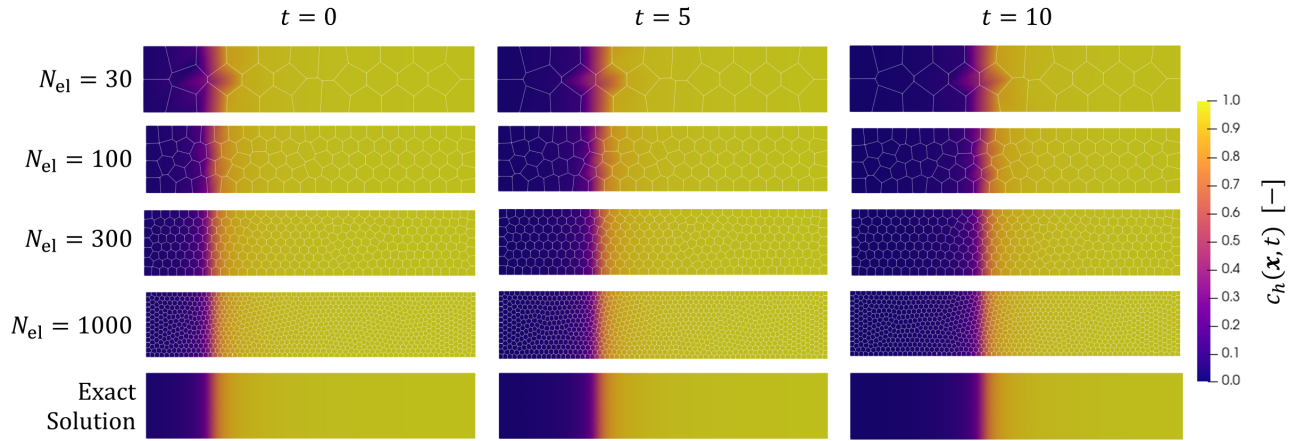
(b) Wavefront propagation of c.

Figure 5: Test case 2: wavefront propagation approximated with $p = 2$.

travelling-wave functions characterized by a velocity of propagation $\bar{v} = 0.1$:

$$c(x,y,t) = \frac{\arctan(3\pi(x - \bar{v}t - 1))}{\pi} + \frac{1}{2}, \qquad q(x,y,t) = \frac{\arctan(-3\pi(x - \bar{v}t - 1))}{\pi} + \frac{1}{2},$$

and we derive forcing terms and Dirichlet conditions accordingly. We adopt the parametrical values in Table 1.

A convergence analysis has been performed as in the previous section, in particular, we collect in Figure 4 the L^2-norm and the DG-norm of the error with respect to the mesh size parameter h. As expected we can observe that the DG-norm of the error decreases as h^p, while the L^2-norm decreases as h^{p+1}.

We repeat the test for two possible final time instants $T_1 = 5$ and $T_2 = 10$. These results aimed at assessing the impact of mesh refinement on the accuracy of the solution where the error is measured in the L^2-norm for various polynomial orders, specifically $p = 1, 2, 3, 4$. The results of our investigations are reported in Table 2. Notably, the L^2-norms of errors at different final time instants are comparable, which supports the fact that the computed solution is stable and correctly approximated. Moreover, with this test, we can highlight the capability of the higher-order methods to accurately replicate the wave behaviour of the solution even with coarser mesh configurations [37]. To illustrate this point, consider the error obtained with $N_{el} = 1000$ and $p = 1$ compared to that with $N_{el} = 300$ and $p = 3$. Even if both setups have the same number of degrees of freedom (3000), the solution approximated with $p = 3$ exhibited an error of 5.29×10^{-4}, which is approximately one order of magnitude smaller than the error in the case $p = 1$ (6.24×10^{-3}). This discrepancy becomes even more evident when comparing the accuracy of the solution achieved with $p = 4$ and $N_{el} = 100$ to that obtained with $p = 2$ and $N_{el} = 300$. Despite having fewer degrees of freedom, the solution computed with $p = 4$ on a coarser mesh is more accurate than the
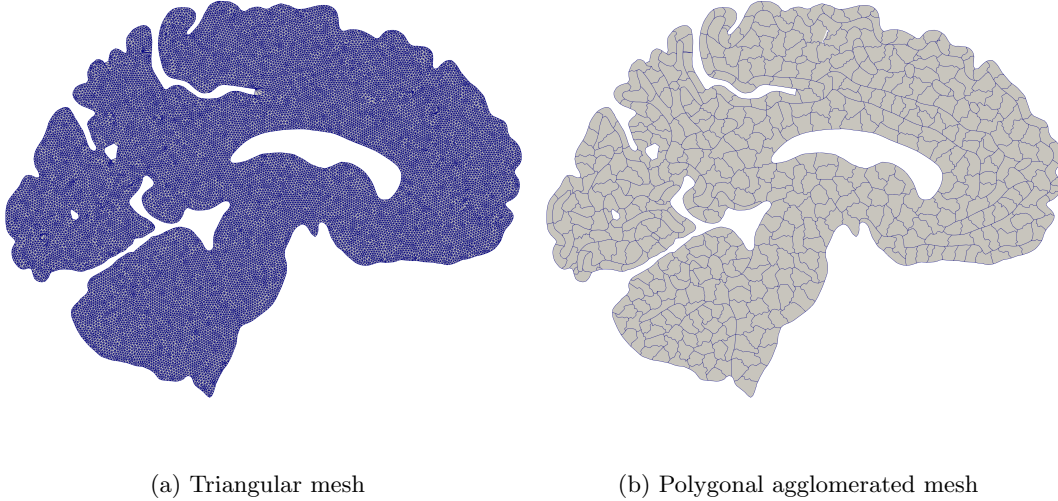
15

| (a) Triangular mesh | (b) Polygonal agglomerated mesh |

Figure 6: Test case 3: Initial (a) and agglomerated (b) meshes of a two-dimensional brain section reconstructed from MRI image.

Parameter	Value		Parameter	Value	
d_ext	10^{-6}	[mm^2/years]	d_axn	0.00	[mm^2/years]
k_0	0.75	[1/years]	k_{12}	1.00	[1/years]
k_1	1.00	[1/years]	$\tilde{k}_1$	0.60	[1/years]

Table 3: Physical parameter values used in Test 3 [16].

one obtained with $p = 2$.

Finally, in Figure 5, we visualize the evolution of the wavefront for the case of $p = 2$ at the two chosen final times, for different levels of mesh refinement. We stress the fact that a sufficiently refined grid is essential to capture the rapid variations characterizing the wave. However, even with $p = 2$, we can confidently conclude that the method produces a numerical solution that accurately reproduces the wave, together with its propagation velocity.

6.3 Test case 3: diffusion processes on agglomerated brain meshes

In this section, we consider a detailed mesh of the brain obtained by segmentation of a structural MRI dataset sourced from the OASIS-3 database [38], as described in [12]. Subsequently, the initial fine triangulated structure, comprising 43402 triangles (of Figure 6a), is agglomerated into a polygonal mesh consisting of 534 elements, of Figure 6b. This transformation gives us the possibility to take full advantage of the versatility of the PolyDG method reducing computational overhead during the simulation.

The goal of this test is to test the capability of the method to correctly reproduce the an isotropic diffusion phenomena on a polygonal agglomerated grid of a brain section. The initial conditions we impose are the following:

$$c_0(x, y) = 0.75 \qquad q_0(x, y) = 0.25e^{-50(x-0.02)^2 - 50y^2}.$$

The values of the model parameters are reported in Table 3. Analysing the model we expect to observe the system to evolve towards the pathological stable equilibrum point presented in Section 2:

$$(c_2, q_2) = \left(\frac{\tilde{k}_1}{k_{12}}, \frac{k_0}{\tilde{k}_1} - \frac{k_1}{k_{12}} \right) = (0.6, 0.25). \tag{22}$$

Moreover, it is possible to compute analytically the minimum speed of the travelling wave solution transitioning the system from the initial solutions towards the pathological state:

$$\bar{v} = 2\sqrt{d_{ext}\left(k_{12}\frac{k_0}{k_1} - \tilde{k}_1 \right)} \simeq 6 \times 10^{-5}.$$
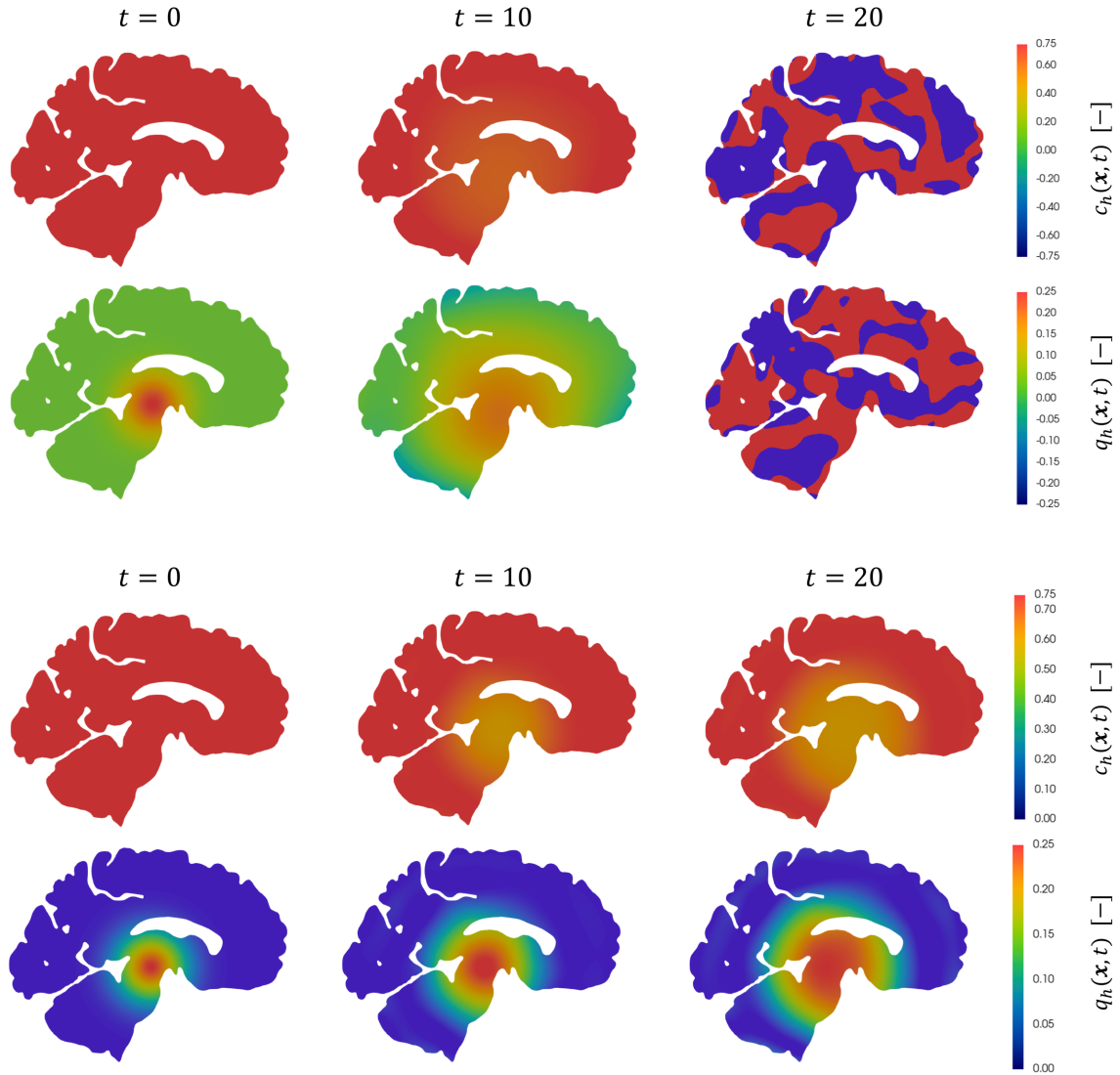
16

Figure 7: Test case 3: Numerical solution obtained by using $p = 2$ (top) and $p = 3$ (bottom).

The problem is coupled with homogeneous Neumann boundary conditions.

In Figure 7, we report screenshots of the approximated solution starting from the initial solution up to final time $T = 20$, $\Delta t = 10^{-2}$ and $p = 2, 3$. Considering the case $p = 2$, we detect an unstable approximated solution, even when employing a reduced time step. Our observations reveal that the employed method lacks positive preservation characteristics. As a consequence, when the approximated solution manifests negative values, the computational scheme converges towards an oscillatory solution with no physical significance. This behavior underscores the need for improved positivity-preserving algorithms in order to maintain the integrity of the numerical solutions in the presence of negative values as in the case of FK model [39].

Nevertheless, stability can be reinstated through the computation of the approximation at a higher order, specifically with $p = 3$, as illustrated in Figures 7. In a reaction-dominated regime, higher-order methods can effectively capture the traveling wave solution, resulting in the recovery of a stable solution transitioning the system towards the stable equilibrium. This behaviour is coherent with the recent results in wave-front simulations studies [37]. This numerical test confirms the capacity of the proposed method of representing the wavefronts in complex geometries, like in brain sections, where the mesh are constructed as agglomeration of detailed triangular meshes, if using sufficiently high order polynomial degree in the approximation. This is a fundamental property to guarantee the quality of the solution in the medical applications.

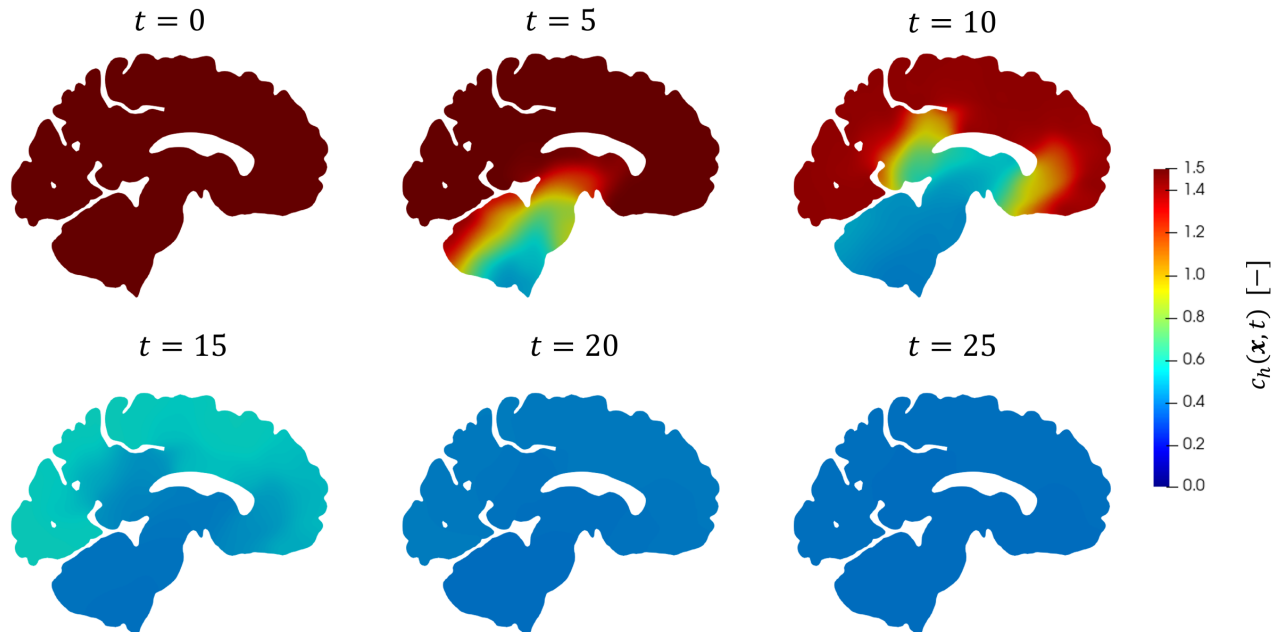| Parameter	Value		Parameter	Value	
d_{ext}	8.00	[mm^2/years]	d_{axn}	80.00	[mm^2/years]
k_0	0.60	[1/years]	k_{12}	1.00	[1/years]
k_1	0.50	[1/years]	$\tilde{k}_1$	0.30	[1/years]

Table 4: Physical parameter values used in Test 4 [16].

Figure 8: The initial configuration corresponds to the unstable healthy state, with a protein concentration of 1.2, uniformily distributed all over the brain. The presence of misfolded proteins trigger the system causing the decay of the concentration.

7 Simulation of α-synuclein spreading in a two dimensional brain section

This Section is devoted to address the problem of simulating the spread of α-synuclein protein into a two dimensional section of the human brain, associated to the Parkinson's disease [7]. Coherently to the modelling of this phenomenon, we impose null flux across the boundary, setting $\partial\Omega = \partial\Omega_{\text{N}}$.

In order to model the diffusion of α-synuclein protein within the previously delineated brain region, we need to establish appropriate parameter configurations. Measuring such mean rate of production, destruction and conversion to provide best-fit coefficients to deterministic model constitutes a developing field in current research [40, 9, 41, 42].

In [12], an exploration of the phenomenon under investigation in this section was conducted through the implementation of the FK model. This model, derived from the heterodimer equations, as elucidated in a prior study [13], offers a simplified representation, focusing on the temporal evolution of the relative concentration of misfolded protein only. The fundamental parameter of interest in this context is the reaction coefficient denoted as α. This parameter holds a phenomenological significance and exhibits a direct connection with the coefficients of the heterodimer model, as established by the following relationship:

$$\alpha = k_{12}\frac{k_0}{k_1} - \tilde{k}_1.$$

Specifically, a significant value for this parameter, one that facilitates the faithful replication of the spreading pattern and propagation velocity of α-synuclein in the brain, may be established at $\alpha = 0.9$/year [13]. Consequently, an appropriate parameter configuration, one that adheres to the relationship delineated in Equation (7) and aligns with the considerations in Section 2. These values are reported in Table 4.
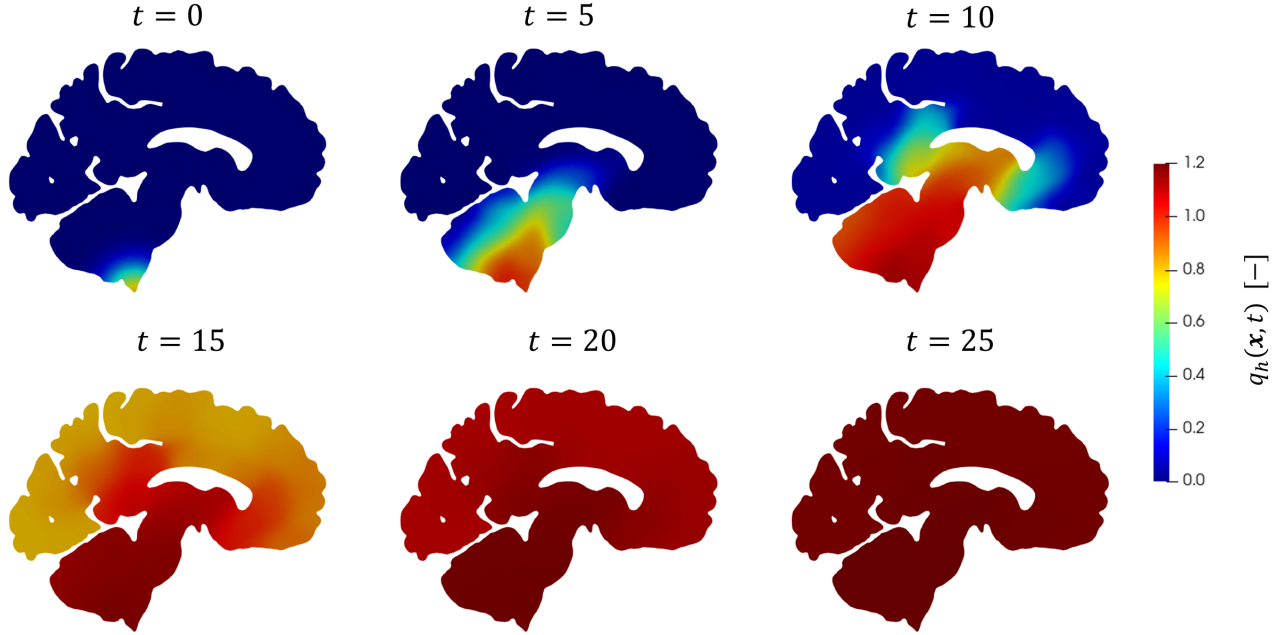
Figure 9: Misfolded protein q_h, initially concentrate into the dorsal motor nucleus, spreads through the entire brain section.

Another important aspect of the model is the construction of the anisotropic part of the diffusion tensor in Equation (2). To fulfill this purpose, the axonal directions $\bar{a}(x)$ are derived from Diffusion Weighted Imaging (DWI) [12]. Moreover we impose an axonal diffusion velocity ten times faster then the isotropic one, as shown in Table 4. We trigger the system with an initial seeding of misfolded version of α-synuclein protein concentrated in the dorsal motor nucleus [43], while we set an initial condition for the healthy protein concentration uniformly equal to the unstable equilibrium point 1.2. We fix the polynomial order $p = 4$ in every element of the discretization, Crank-Nicolson method for the time discretization with time step $\Delta t = 0.01$ and simulate up to $T = 25$ years. We have opted for a second-order numerical method in order to ensure the accurate approximation of the wavefront over an extended temporal simulation interval. This selection is motivated by the need to maintain precision and stability in modeling the wave's behavior over a protracted time span.

In this framework we expect the system to develop from the initial state towards the stable equilibrium point $(c_h, q_h) = (0.3, 1.5)$. In Figures 8 and 9, we report the approximated solution at different time instants of the simulation. The solutions have effectively developed toward a stable pathological state. We compare the misfolded evolution in Figure 9 with the solution obtained in other works in literature [12, 39]. The preceding investigation applied the FK equation and despite minor discrepancies arising from the distinct diffusion tensor employed, our analysis reveals a prevailing alignment in the propagation directions of the misfolded protein. Starting from the motor nucleus the misfolded protein spread towards the lower brain stem, subsequently ascending to involve the cerebral cortex in the advanced stages of the pathological process. This observed activation pattern within distinct brain regions aligns with the theoretical tenets elucidated in the Braak staging theory [44].

8   Conclusions

In this article, we have introduced a Polygonal Discontinuous Galerkin method as a computational approach for simulating the heterodimer model, applied to the description of the dynamics of α-synuclein proteins in Parkinson's disease, considering both the evolution of healthy and misfolded toxic states. Our work includes demonstrating the stability of the numerical solution and establishing an error estimate for the semi-discrete solution. We have validated the theoretical convergence rate through a convergence analysis with respect to mesh refinements. Furthermore, we have conducted a numerical examination to confirm the exponential convergence of the error with respect to the order of approximation p, even though this aspect was not explicitly addressed in our theoretical analysis. Finally, we have numerically verified the theoretical convergence rate with respect to time discretization

methods, specifically Backward Euler and Crank-Nicolson, for addressing the temporal aspects of the problem. Then, we have accessed the ability of the method to accurately reproduce a traveling-wave solution. Our findings have affirmed the method's ability to accurately reconstruct the propagation front of the solution, particularly when higher-order methods are employed, even on coarser grids.

We have applied the analyzed model to reproduce the diffusion processes in a two-dimensional brain section. In the isotropic diffusions test it has become more evident the necessity of employing high-order numerical methods to achieve a stable solution that faithfully replicated the propagation of the traveling wave transitioning the system towards the pathological state. In the end, we have conducted simulations to replicate the anisotropic spreading of α-synuclein across the brain section, in Parkinson's disease. Our results have been validated by comparing them with simulations based on the Fisher-Kolmogorov equation and clinical data from the literature regarding the evolution of this protein in Parkinson's disease. In conclusion, the heterodimer model has demonstrated its utility as a valuable tool for advancing research in the mathematical modeling of neurodegenerative diseases.

A logical progression of our research involves extending its application to a three-dimensional representation of the brain, aimed at offering a comprehensive understanding of the intricate dynamics of protein interactions and their spread within a more realistic brain environment. Furthermore, an additional prospective direction involves conducting a comprehensive quantitative analysis of the influence exerted by all the parameters within the system on the solution. In this way the numerical method may serve as a useful tool, supporting the medical research efforts aimed at investigating potential therapeutic treatments for neurodegenerative diseases by targeting the molecular reactions that prions undergo. The heterodimer model can also find application in the study of other prion-like proteins, such as β-amyloid and tau proteins, which are pivotal in Alzheimer's disease. The extension of its applicability enriches our comprehension of neurodegenerative conditions and contributes to the progression toward more precise and less invasive patient-specific healthcare approaches.

Acknowledgments

Declaration of competing interests

The authors declare that they have no known competing financial interests or personal relationships that could have appeared to influence the work reported in this article.

References

[1] M. Jucker and L. C. Walker, "Self-propagation of pathogenic protein aggregates in neurodegenerative diseases," *Nature*, vol. 501, no. 7465, pp. 45–51, 2013.

[2] D. M. Wilson, M. R. Cookson, L. Van Den Bosch, H. Zetterberg, D. M. Holtzman, and I. Dewachter, "Hallmarks of neurodegenerative diseases," *Cell*, vol. 186, no. 4, pp. 693–714, 2023.

[3] J. M. Tarasoff-Conway, R. O. Carare, R. S. Osorio, L. Glodzik, T. Butler, E. Fieremans, L. Axel, H. Rusinek, C. Nicholson, B. V. Zlokovic, B. Frangione, K. Blennow, J. Ménard, H. Zetterberg, T. Wisniewski, and M. J. de Leon, "Clearance systems in the brain—implications for Alzheimer disease," *Nature reviews. Neurology*, vol. 11, no. 8, pp. 457–470, 2015.

[4] M. Hasegawa, T. Nonaka, and M. Masuda-Suzukake, "Prion-like mechanisms and potential therapeutic targets in neurodegenerative disorders," *Pharmacology & Therapeutics*, vol. 172, pp. 22–33, 2017.

[5] J. Weickenmeier, E. Kuhl, and A. Goriely, "Multiphysics of Prionlike Diseases: Progression and Atrophy," *Physical Review Letters*, vol. 121, no. 15, p. 158101, 2018.

[6] J. M. George, "The synucleins," *Genome Biology*, vol. 3, no. 1, p. reviews3002, 2002.

[7] M. G. Spillantini, M. L. Schmidt, V. M.-Y. Lee, J. Q. Trojanowski, R. Jakes, and M. Goedert, "α-Synuclein in Lewy bodies," *Nature*, vol. 388, no. 6645, pp. 839–840, 1997.

[8] S. Korat, N. S. R. Bidesi, F. Bonanno, A. Di Nanni, A. N. N. Hoàng, K. Herfert, A. Maurer, U. M. Battisti, G. D. Bowden, D. Thonon, D. Vugts, A. D. Windhorst, and M. M. Herth, "Alpha-Synuclein PET tracer development-an overview about current efforts," *Pharmaceuticals*, vol. 14, no. 9, p. 847, 2021.

[9] J. Masel, V. A. A. Jansen, and M. A. Nowak, "Quantifying the kinetic parameters of prion replication," *Biophysical Chemistry*, vol. 77, no. 2, pp. 139–152, 1999.

[10] F. Carbonell, Y. Iturria-Medina, and A. C. Evans, "Mathematical modeling of protein misfolding mechanisms in neurological diseases: a historical overview," *Frontiers in Neurology*, vol. 9, 2018.

[11] F. Matthäus, "Diffusion versus network models as descriptions for the spread of prion diseases in the brain," *Journal of Theoretical Biology*, vol. 240, no. 1, pp. 104–113, 2006.

[12] M. Corti, F. Bonizzoni, L. Dede', A. M. Quarteroni, and P. F. Antonietti, "Discontinuous Galerkin methods for Fisher–Kolmogorov equation with application to *alpha*-synuclein spreading in Parkinson's disease," *Computer Methods in Applied Mechanics and Engineering*, vol. 417, p. 116450, 2023.

[13] J. Weickenmeier, M. Jucker, A. Goriely, and E. Kuhl, "A physics-based model explains the prion-like features of neurodegeneration in Alzheimer's disease, Parkinson's disease, and amyotrophic lateral sclerosis," *Journal of the Mechanics and Physics of Solids*, vol. 124, pp. 264–281, 2019.

[14] S. Fornari, A. Schäfer, M. Jucker, A. Goriely, and E. Kuhl, "Prion-like spreading of Alzheimer's disease within the brain's connectome," *Journal of The Royal Society Interface*, vol. 16, no. 159, p. 20190356, 2019.

[15] B. Franchi and S. Lorenzani, "From a microscopic to a macroscopic model for Alzheimer disease: Two-scale homogenization of the Smoluchowski equation in perforated domains," *Journal of Nonlinear Science*, vol. 26, p. 717–753, 2016.

[16] T. B. Thompson, P. Chaggar, E. Kuhl, A. Goriely, and f. t. A. D. N. Initiative, "Protein-protein interactions in neurodegenerative diseases: A conspiracy theory," *PLOS Computational Biology*, vol. 16, no. 10, p. e1008267, 2020.

[17] A. Cangiani, Z. Dong, E. H. Georgoulis, and P. Houston, *hp-Version Discontinuous Galerkin Methods on Polygonal and Polyhedral Meshes*. Springer International Publishing, 2017.

[18] P. F. Antonietti, N. Farenga, E. Manuzzi, G. Martinelli, and L. Saverio, "Agglomeration of polygonal grids using graph neural networks with applications to multigrid solvers," 2022, arXiv:math.NA/2210.17457.

[19] S. B. Prusiner, "Novel proteinaceous infectious particles cause scrapie," *Science*, vol. 216, no. 4542, pp. 136–144, 1982.

[20] S. B. Prusiner, "Molecular biology of prion diseases," *Science*, vol. 252, no. 5012, pp. 1515–1522, 1991.

[21] J. D. Harper and P. T. Lansbury, "Models of amyloid seeding in Alzheimer's disease and scrapie: Mechanistic truths and physiological consequences of the time-dependent solubility of amyloid proteins," *Annual Review of Biochemistry*, vol. 66, no. 1, pp. 385–407, 1997.

[22] D. A. Harris, "Cellular biology of prion diseases," *Clinical Microbiology Reviews*, vol. 12, no. 3, pp. 429–444, 1999.

[23] M. Eigen, "Prionics or the kinetic basis of prion diseases," *Biophysical Chemistry*, vol. 63, no. 1, pp. A1–A18, 1996.

[24] A. Cangiani, E. H. Georgoulis, and P. Houston, "hp-version discontinuous Galerkin methods on polygonal and polyhedral meshes," *Mathematical Models and Methods Applied Sciences*, vol. 24, no. 10, pp. 2009–2041, 2014.

[25] P. F. Antonietti, A. Cangiani, J. Collis, Z. Dong, E. H. Georgoulis, S. Giani, and P. Houston, "Review of discontinuous Galerkin finite element methods for partial differential equations on complicated domains," in *Building Bridges: Connections and Challenges in Modern Approaches to Numerical Partial Differential Equations*, pp. 281–310, Springer International Publishing, 2016.

[26] P. F. Antonietti, F. Brezzi, and L. D. Marini, "Bubble stabilization of discontinuous Galerkin methods," *Computer Methods in Applied Mechanics and Engineering*, vol. 198, no. 21, pp. 1651–1659, 2009.

[27] D. A. Di Pietro and J. Droniou, *The Hybrid High-Order Method for Polytopal Meshes: Design, Analysis, and Applications.* Springer, 2020.

[28] A. Buffa and C. Ortner, "Compact embeddings of broken Sobolev spaces and applications," *IMA Journal of Numerical Analysis*, vol. 29, no. 4, pp. 827–855, 2009.

[29] P. A. Gazca-Orozco and A. Kaltenbach, "On the $L^\infty(0, T; L^2(\Omega)^d)$-stability of discontinuous Galerkin schemes for incompressible flows," 2023, arXiv:math.NA/2301.02077.

[30] D. N. Arnold, F. Brezzi, B. Cockburn, and L. D. Marini, "Unified analysis of discontinuous Galerkin methods for elliptic problems," *SIAM Journal on Numerical Analysis*, vol. 39, no. 5, pp. 1749–1779, 2002.

[31] A. Quarteroni, *Numerical Models for Differential Problems.* Springer, 3 ed., 2017.

[32] J. R. L. Webb, "Extensions of Gronwall's inequality with quadratic growth terms and applications," *Electronic Journal of Qualitative Theory of Differential Equations*, vol. 61, pp. 1–12, 2018.

[33] I. Babuška and M. Suri, "The p and h-p versions of the finite element method, basic principles and properties," *SIAM review*, vol. 36, no. 4, pp. 578–632, 1994.

[34] B. Rivière, "Discontinuous Galerkin methods for solving elliptic and parabolic equations - theory and implementation," in *Frontiers in Applied Mathematics*, 2008.

[35] P. F. Antonietti, S. Bonetti, M. Botti, M. Corti, I. Fumagalli, and I. Mazzieri, "Lymph: an efficient high-order solver for differential problems with polytopal discontinuous Galerkin methods," 2023, in preparation.

[36] C. Talischi, G. H. Paulino, A. Pereira, and I. F. M. Menezes, "PolyMesher: a general-purpose mesh generator for polygonal elements written in Matlab," *Structural and Multidisciplinary Optimization*, vol. 45, no. 3, pp. 309—-328, 2012.

[37] P. F. Antonietti, M. Botti, and I. Mazzieri, "On mathematical and numerical modelling of multiphysics wave propagation with polytopal discontinuous Galerkin methods: a review," *Vietnam Journal of Mathematics*, vol. 50, no. 4, pp. 997–1028, 2022.

[38] P. J. LaMontagne, T. L. Benzinger, J. C. Morris, S. Keefe, R. Hornbeck, C. Xiong, E. Grant, J. Hassenstab, K. Moulder, A. G. Vlassenko, M. E. Raichle, C. Cruchaga, and D. Marcus, "OASIS-3: Longitudinal neuroimaging, clinical, and cognitive dataset for normal aging and Alzheimer disease," *medRxiv*, 2019.

[39] M. Corti, F. Bonizzoni, and P. F. Antonietti, "Structure preserving polytopal discontinuous Galerkin methods for the numerical modeling of neurodegenerative diseases," 2023, arXiv:math.NA/2308.00547.

[40] Z. R. Li, G. R. Liu, and D. Mi, "Quantifying the parameters of Prusiner's heterodimer model for prion replication," *Physica A: Statistical Mechanics and its Applications*, vol. 346, no. 3, pp. 459–474, 2005.

[41] M. Iljina, G. A. Garcia, M. H. Horrocks, L. Tosatto, M. L. Choi, K. A. Ganzinger, A. Y. Abramov, S. Gandhi, N. W. Wood, N. Cremades, C. M. Dobson, T. P. J. Knowles, and D. Klenerman, "Kinetic model of the aggregation of alpha-synuclein provides insights into prion-like spreading," *Proceedings of the National Academy of Sciences*, vol. 113, no. 9, pp. E1206–E1215, 2016.

[42] G. Perrino, C. Wilson, M. Santorelli, and D. di Bernardo, "Quantitative characterization of α-synuclein aggregation in living cells through automated microfluidics feedback control," *Cell Reports*, vol. 27, no. 3, pp. 916–927.e5, 2019.

[43] D. W. Dickson, "Neuropathology of Parkinson disease," *Parkinsonism & Related Disorders*, vol. 46, pp. S30–S33, 2018.

[44] H. Braak, K. D. Tredici, U. Rüb, R. A. I. de Vos, E. N. H. Jansen Steur, and E. Braak, "Staging of brain pathology related to sporadic Parkinson's disease," *Neurobiology of Aging*, vol. 24, no. 2, pp. 197–211, 2003.

MOX Technical Reports, last issues

77/2023 Fumagalli, I.; Corti, M.; Parolini, N.; Antonietti, P. F.
Polytopal discontinuous Galerkin discretization of brain multiphysics flow dynamics

76/2023 Ieva, F.; Galliani, G.; Secchi, P.
The impact of public transport on the diffusion of COVID-19 pandemie in Lombardy during 2020

74/2023 Pidò, S.; Pinoli, P.; Crovari, P.; Ieva, F.; Garzotto, F.; Ceri, S.
Ask Your Data—Supporting Data Science Processes by Combining AutoML and Conversational Interfaces

75/2023 Archetti, A.; Ieva, F.; Matteucci, M.
Scaling survival analysis in healthcare with federated survival forests: A comparative study on heart failure and breast cancer genomics

71/2023 Conni, G.; Piccardo, S.; Perotto, S.; Porta, G.M.; Icardi, M.
HiPhome: HIgh order Projection-based HOMogEnisation for advection diffusion reaction problems

70/2023 Ragni, A.; Ippolito, D.; Masci, C.
Assessing the Impact of Hybrid Teaching on Students' Academic Performance via Multilevel Propensity Score-based techniques

69/2023 Ferro, N.; Micheletti, S.; Parolini, N.; Perotto, S.; Verani, M.; Antonietti, P. F.
Level set-fitted polytopal meshes with application to structural topology optimization

68/2023 Vitullo, P.; Colombo, A.; Franco, N.R.; Manzoni, A.; Zunino, P.
Nonlinear model order reduction for problems with microstructure using mesh informed neural networks

67/2023 Conti, P.; Guo, M.; Manzoni, A.; Hesthaven, J.S.
Multi-fidelity surrogate modeling using long short-term memory networks

66/2023 Fresca, S.; Gobat, G.; Fedeli, P.; Frangi, A.; Manzoni, A.
Deep learning-based reduced order models for the real-time simulation of the nonlinear dynamics of microstructures